Diamond & Related Materials 169 (2026) 114035

Contents lists available at ScienceDirect

Diamond & Related Materials

journal homepage: www.elsevier.com/locate/diamond

Acoustoelectric conversion efficiency in fluorine-doped single-walled carbon nanotubes☆

D. Sekyi-Arthur [a,c,*], K.A. Dompreh [b], F. Amo-Mensah [a], S.Y. Mensah [b], B. Afoakwa [a,c]

[a] Department of Physics, College of Basic and Applied Sciences, University of Ghana, PMB, Accra, Ghana
[b] Department of Physics, College of Agriculture and Natural Sciences, University of Cape Coast, PMB, Cape Coast, Ghana
[c] Centre for Quantum Transport in Advanced Materials, University of Ghana, PMB, Accra, Ghana

ARTICLE INFO

Keywords:
Acoustoelectric conversion efficiency
Carbon nanotubes
Bloch oscillations
Boltzmann transport equation
Electron–phonon interaction
Nonlinear field effects

ABSTRACT

This study presents a comprehensive theoretical investigation of the acoustoelectric conversion efficiency (η) in fluorine-doped single-walled carbon nanotubes (FSWCNTs) subjected to combined dc and ac electric fields in the hypersound regime ($q\ell \gg 1$). A microscopic transport model is developed within the semiclassical Boltzmann transport formalism by incorporating electron–phonon interactions, Bloch oscillations, nonlinear field modulation, and temperature-dependent carrier scattering. Analytical expressions for the acoustoelectric current density (J_{AE}) and the corresponding conversion efficiency are derived, while the electronic and lattice properties are discussed within the framework of density functional perturbation theory (DFPT) to establish the microscopic origin of the transport parameters. The model explicitly accounts for the effects of nanotube chirality, axial and circumferential overlap integrals (Δ_z and Δ_s), carrier relaxation time, nanotube length, carrier concentration, and fluorination-induced lattice modifications. The results reveal that the acoustoelectric conversion efficiency increases approximately linearly with the applied dc electric field and exhibits pronounced resonant enhancements whenever the Bloch frequency approaches integer multiples of the applied ac frequency. The oscillatory dependence on the ac field amplitude originates from multiphoton-assisted sideband formation described by Bessel-function modulation of the carrier dynamics. The conversion efficiency displays a non-monotonic temperature dependence with a well-defined optimum temperature arising from the competition between thermally activated carrier transport and enhanced electron–phonon scattering. A detailed sensitivity analysis demonstrates that increasing the phenomenological damping factor broadens the resonance linewidth, suppresses the peak conversion efficiency, and reduces the resonance quality factor without significantly shifting the resonance frequency, thereby confirming that damping primarily governs carrier coherence rather than the intrinsic Bloch dynamics. The analysis further shows that electron–phonon scattering, impurity scattering, fluorine-induced lattice disorder, and phonon lifetime collectively determine the effective relaxation rate and consequently the efficiency of acoustoelectric energy conversion. Furthermore, the axial overlap integral, nanotube length, carrier concentration, and carrier relaxation time are identified as the dominant parameters controlling the acoustoelectric response. Enhanced conversion efficiency is obtained under conditions of low damping, long carrier relaxation times, optimised Bloch frequency, and moderate fluorination, where coherent momentum transfer between acoustic phonons and charge carriers is maximised. These findings provide a comprehensive physical framework for understanding resonant acoustoelectric transport in fluorinated carbon nanotubes and offer practical design guidelines for developing high-efficiency nanoscale acoustoelectric energy harvesters, high-frequency sensors, phononic devices, and next-generation nanoelectromechanical systems.

☆ This work is licensed under the Creative Commons Attribution International License (CC BY). http://creativecommons.org/licenses/by/4.0/.
* Corresponding author.
E-mail address: dsekyi-arthur@ug.edu.gh (D. Sekyi-Arthur).
URL: http://www.ug.edu.gh/physics (D. Sekyi-Arthur).

https://doi.org/10.1016/j.diamond.2026.114035
Received 6 November 2025; Received in revised form 13 July 2026; Accepted 30 July 2026
Available online 5 August 2026
0925-9635/© 2026 Elsevier B.V. All rights are reserved, including those for text and data mining, AI training, and similar technologies.

1. Introduction

Acoustodynamics refers to the generation of a direct current in a semiconductor due to the drag of charge carriers by co-propagating acoustic waves, which is mediated by electron–phonon momentum exchange [1,2]. This phenomenon, which was first observed by Parmenter [2], has attracted renewed attention in novel low-dimensional systems, where quantum confinement enhances carrier–phonon coupling. In recent years, acoustoelectric conversion has been explored in piezoelectric semiconductors, graphene, superlattices, and single-walled carbon nanotubes (SWCNTs) [3,4].

Owing to their quasi–one–dimensional structure, SWCNT possess a high carrier mobility, and strong electron–phonon interaction, which offers a unique platform for investigating acoustoelectric transport metrics. Earlier experiments have reported on acoustoelectric currents in SWCNT bundles under radio-frequency acoustic excitation [5], whereas subsequent studies observed quantised acoustoelectric currents using surface acoustic waves [6]. However, theoretical models have since been extended to degenerate [4] and functionalised nanotubes [7], which highlights the influence of chirality and doping on the acoustoelectric response.

Functionalisation of nanotubes, such as fluorine doping of SWCNTs, is a key tuning parameter in modifying carrier concentration and electron–phonon coupling, and also managing the impacts of nonlinear transport; strong electric fields, acoustic phonons, and fluorine doping can interact to provide novel nonlinear transport effects that are crucial for next-generation nanoelectronic uses [7].

A central mechanism in SWCNT acoustoelectric systems is the interplay between Bloch oscillations of electrons in periodic potentials and the sideband mixing induced by ac fields. Bloch oscillations have been experimentally observed in a variety of photonic and phononic systems, and were initially predicted for electrons in crystals under a constant force [8–11]. When the Bloch frequency ω_B coincides with integer multiples of the ac driving frequency ω, resonance takes place in acoustoelectric systems, resulting in improved energy transfer [12,13]. Such resonant behaviour, modulated by carrier relaxation time τ, has analogies in SWCNT transport and provides a route to tunable high-frequency acoustoelectric conversion.

However, it is noteworthy that, as far as we are aware, no prior study has been conducted on the acoustoelectric conversion efficiency in FSWCNTs. Therefore, our main objective is to examine and evaluate the semiclassical acoustoelectric conversion efficiency of FSWCNTs and their possible use in next-generation electronic systems.

Despite extensive progress, several challenges still remain unresolved. The influence of temperature-dependent scattering on acoustoelectric efficiency, the role of geometric parameters such as overlap integrals (Δ_s, Δ_z) and chirality, and the nonlinear modulation of Bessel sidebands under strong ac fields remain incompletely understood [14,15]. Bridging the gap between simplified models and experimental data, therefore, requires a comprehensive framework that integrates Bloch resonance, nonlinear field effects, and phonon damping.

In the current study, we present a semiclassical Boltzmann-based model for the acoustoelectric conversion efficiency η in FSWCNTs driven by combined dc and ac electric fields. The model accounts for Bloch oscillations, space charge instabilities, nonlinear modulation, thermal scattering, and the geometric configuration of the FSWCNT. Analytical expressions for the acoustoelectric current density and conversion efficiency η are derived and analysed. The results demonstrate quasi-linear growth of η with dc bias, resonant peaks at $\omega_B = n\omega$, oscillatory dependence on ac amplitude α, non-monotonic temperature behaviour with an optimal T^*, and sensitivity to overlap integrals and tube length.

These findings provide a coherent theoretical basis for optimising FSWCNT-based acoustoelectric devices for nanoscale energy harvesting, self-powered nanoelectronics, acoustic sensors, radio-frequency signal processing, phononic computing, nanoelectromechanical systems (NEMS), Internet-of-Things (IoT) devices, and acoustic wave amplifiers.

Fig. 1 shows the schematic illustration of the FSWCNT acoustoelectric device considered in this work. A surface acoustic wave (SAW) with wave vector **q** propagates along the nanotube axis while combined dc ($\mathcal{E}_0$) and ac ($\mathcal{E}_1 \cos\omega t$) electric fields drive the electron transport. Fluorine adatoms modify the electronic band structure and electron–phonon interaction, thereby enhancing the acoustoelectric conversion efficiency. The nanotube length used in the simulations is $L = 200$ nm with a typical diameter of 1.2–1.5 nm.

2. Theory

The study was carried out in the semiclassical regime, where the energy dispersion relation for the FSWCNT is modelled using the Huckel matrix approximation as [7,16–19]:

$$\vartheta(p) = \vartheta_o - \Delta_s \cos\left(\frac{p_s d_s}{\hbar}\right) - \Delta_z \cos\left(\frac{p_z d_z}{\hbar}\right). \tag{1}$$

Here $d_s = \sqrt{3}b_s/2$ and $d_z = 3\sqrt{3}b_z/2$, with $b_{s,z}$ being the carbon–carbon bond lengths along the helical base and tubular axis, respectively. These parameters Δ_s and Δ_z are real-valued overlap integrals, and correspond to carrier transitions along the spiral and axial directions.

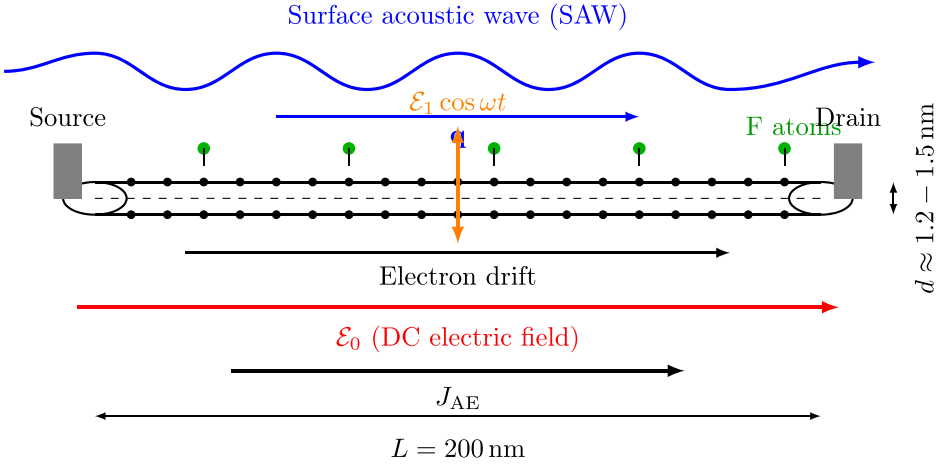


Fig. 1. Schematic illustration of the FSWCNT acoustoelectric device considered in this work. A surface acoustic wave (SAW) with wave vector **q** propagates along the nanotube axis while combined dc ($\mathcal{E}_0$) and ac ($\mathcal{E}_1 \cos\omega t$) electric fields drive the electron transport. Fluorine adatoms modify the electronic band structure and electron–phonon interaction, thereby enhancing the acoustoelectric conversion efficiency. The nanotube length used in the simulations is $L = 200$ nm with a typical diameter of 1.2–1.5 nm.

Table 1
Representative values of the axial (Δ_z) and circumferential (Δ_s) overlap integrals reported in the literature for carbon nanotubes. The values reported for the semiclassical miniband model correspond to effective transport parameters rather than the atomistic nearest-neighbour hopping energy.

Method	Δ_z (eV)	Δ_s (eV)	Physical basis	References
Graphene TBA	2.7	2.7	Nearest-neighbour hopping parameter (γ_0)	[20,25]
DFT (large SWCNT)	2.7–2.9	2.6–2.8	First-principles calculations including curvature effects	[26,28]
Chiral–SWCNT(DFT)	2.7–2.9	2.5–2.8	Chirality-dependent electronic coupling	[20]
F–SWCNT (DFT)	1.5–2.6	1.2–2.5	Reduction of π-orbital overlap due to C–F bond formation and partial $sp^2 \rightarrow sp^3$ rehybridization	[21,22]
Semiclassical–miniband transport model	0.02–0.10	0.02–0.10	Effective miniband overlap parameters used in Boltzmann transport theory	[23]

2.1. Material parameters of fluorine-doped single-walled carbon nanotubes

The electronic transport properties of FSWCNTs depend strongly upon the carrier concentration, nearest-neighbour overlap integrals and electron–phonon coupling strength. Unlike pristine carbon nanotubes, these parameters are modified by the formation of covalent carbon–fluorine bonds, which perturb the electronic structure through charge transfer and local lattice distortion [20–22].

Fluorine possesses the largest electronegativity of any element ($\chi_F = 3.98$) on the Pauling scale. When fluorine atoms bond to the nanotube surface, electrons are transferred from neighbouring carbon atoms towards the fluorine atoms. This redistribution of charge modifies the local electrostatic potential, changes the occupation of the π orbitals and partially transforms the carbon bonding configuration from sp^2 towards sp^3 hybridisation.

Within the tight-binding approximation, the electronic Hamiltonian may be written as

$$\mathcal{H} = \sum_i \varepsilon_i c_i^\dagger c_i + \sum_{\langle i,j \rangle} t_{ij} c_i^\dagger c_j, \tag{2}$$

where ε_i denotes the on-site energy, t_{ij} represents the nearest-neighbour hopping energy, and $c_i^\dagger$ and c_i are the electron creation and annihilation operators. For fluorinated nanotubes,

$$t_{ij} \rightarrow t_{ij}^{(F)}, \tag{3}$$

owing to the modified carbon–carbon bond lengths and local electronic environment introduced by the C–F bonds. Accordingly, the overlap integrals employed in the present work, Δ_s and Δ_z, represent effective hopping parameters describing electron motion in the circumferential and axial directions of the nanotube [20,23–25]. Fluorination changes these overlap integrals according to $\Delta_s = \Delta_s^{(0)} + \delta\Delta_s$, and $\Delta_z = \Delta_z^{(0)} + \delta\Delta_z$, where $\delta\Delta_s$, $\delta\Delta_z$ describe the perturbations induced by fluorine incorporation. Similarly, the equilibrium carrier concentration changes from

$$n_0^{(0)} \longrightarrow n_0^{(F)}, \tag{4}$$

because fluorination shifts the Fermi level through charge transfer. The carrier concentration satisfies $n_0 = \int D(E) f(E)\, dE$, since fluorination modifies both the density of states and the electronic dispersion relation, the resulting carrier concentration differs from that of pristine SWCNTs. The numerical values employed in the present work were selected from published experimental measurements and density-functional-theory calculations reported for fluorinated carbon nanotubes [21,22,26,27]. These investigations demonstrate that fluorination alters the hopping parameters, carrier density and electron–phonon interaction strength while preserving the quasi-one-dimensional nature of the nanotube (see Table 1).

Consequently, the transport model employed here is specifically parameterised for fluorinated SWCNTs rather than pristine nanotubes. The carrier density employed throughout this work is treated as an effective three-dimensional density for consistency with the semiclassical Boltzmann transport formalism. Although an isolated SWCNT is intrinsically quasi-one-dimensional, the equivalent one-dimensional carrier density may be written as $n_{1D} = n_{3D} A$, where $A = \pi d t$ is the effective nanotube cross-sectional area.

The high-frequency acoustoelectric current density deduced previously in Refs. [15,29] is separated into axial and circumferential components as:

$$\begin{aligned} J_z = \frac{J_{0z}}{2} \Bigg[& 1 + \sum_{k=-\infty}^{\infty} \frac{J_k^2(z')}{1 + \left(2\Omega\tau + k\omega\tau\right)^2} \\ & - \frac{8\cos A}{\Delta_s} \sin\!\left(\frac{q d_z}{2}\right) \sum_{k=-\infty}^{\infty} \frac{J_k^2(z)\left(\Omega\tau + k\omega\tau\right)}{1 + \left(\Omega\tau + k\omega\tau\right)^2} \Bigg] \\ + \frac{J_{0s}}{2} \Bigg[& 1 + \sum_{k=-\infty}^{\infty} \frac{J_k^2(z')}{1 + \left(2\Omega\tau + k\omega\tau\right)^2} \\ & - \frac{8\cos A}{\Delta_s} \sin\!\left(\frac{q d_s}{2}\right) \sum_{k=-\infty}^{\infty} \frac{J_k^2(z)\left(\Omega\tau + k\omega\tau\right)}{1 + \left(\Omega\tau + k\omega\tau\right)^2} \Bigg] \sin^2\theta, \end{aligned} \tag{5}$$

and

$$\begin{aligned} J_s = \frac{J_{0s}}{2} \Bigg[& 1 + \sum_{k=-\infty}^{\infty} \frac{J_k^2(z')}{1 + \left(2\Omega\tau + k\omega\tau\right)^2} \\ & - \frac{8\cos A}{\Delta_s} \sin\!\left(\frac{q d_s}{2}\right) \sum_{k=-\infty}^{\infty} \frac{J_k^2(z)\left(\Omega\tau + k\omega\tau\right)}{1 + \left(\Omega\tau + k\omega\tau\right)^2} \Bigg] \sin\theta\cos\theta, \end{aligned} \tag{6}$$

where $z' \equiv 2z = 2e\mathcal{E}_1 d_s/\omega$, $\Omega = e\mathcal{E}_0 d_{s,z}/\hbar$, and $J_k(\cdot)$ denotes the Bessel function of the first kind. From Eq. (5), we group and isolate harmonic contributions by defining a bracket function (depending on geometric length $d \in \{d_z, d_s\}$):

$$\begin{aligned} \mathcal{B}(d;\tau) \equiv 1 + & \sum_{k=-\infty}^{\infty} \frac{J_k^2(z')}{1 + \left(2\Omega\tau + k\omega\tau\right)^2} \\ & - \frac{8\cos A}{\Delta_s} \sin\!\left(\frac{qd}{2}\right) \sum_{k=-\infty}^{\infty} \frac{J_k^2(z)\left(\Omega\tau + k\omega\tau\right)}{1 + \left(\Omega\tau + k\omega\tau\right)^2}. \end{aligned} \tag{7}$$

Thus, Eq. (5) is compactly written as

$$J_z = \frac{J_{0z}}{2}\, \mathcal{B}(d_z;\tau) + \frac{J_{0s}}{2}\, \mathcal{B}(d_s;\tau)\, \sin^2\vartheta. \tag{8}$$

The harmonic (Bessel-weighted) contribution to the dc (time-averaged) acoustoelectric current is contained in the sums inside $\mathcal{B}(\cdot)$. We therefore isolate the harmonic sum component as:

$$S_{\mathrm{harm}}(\tau) \equiv \sum_{k=-\infty}^{\infty} \left[J_k^2(z')\, R_k^{(1)}(\tau) + J_k^2(z)\, R_k^{(2)}(d;\tau) \right], \tag{9}$$

with the rational response functions obtained as

$$R_k^{(1)}(\tau) \equiv \frac{1}{1+\left(2\Omega\tau + k\omega\tau\right)^2}, \tag{10}$$

$$R_k^{(2)}(d;\tau) \equiv -\frac{8\cos A}{\Delta_s}\sin\!\left(\frac{qd}{2}\right)\frac{\Omega\tau + k\omega\tau}{1+\left(\Omega\tau + k\omega\tau\right)^2}. \tag{11}$$

Thus, the harmonic part of J_z may be written exactly as

$$J_{AE} \;=\; \left(\frac{J_{0z}}{2} + \frac{J_{0s}}{2}\sin^2\theta\right) S_{\rm harm}(\tau), \tag{12}$$

where the additive constant terms (i.e., "1"s in $\mathcal{B}$) may be treated as baseline offsets and do not contribute to the Bessel-harmonic spectral structure of interest.

We reindex into a single spectral sum by assuming that both sums in Eq. (9) run over the same integer index set and thus, $k \to n$ to emphasise a single spectral sum as:

$$S_{\rm harm}(\tau) = \sum_{n=-\infty}^{\infty}\left[J_n^2(z')\,\mathcal{L}_n^{(1)}(\tau) + J_n^2(z)\,\mathcal{L}_n^{(2)}(d;\tau)\right], \tag{13}$$

where $\mathcal{L}_n^{(1)} \equiv R_n^{(1)}$ and $\mathcal{L}_n^{(2)} \equiv R_n^{(2)}$ for brevity. At this juncture everything is exact, and $S_{\rm harm}$ is the sum of the two Bessel-weighted response series.

We avoid complexity by mapping the two sums into a single effective spectral sum. The compact form of the acoustoelectric current density along the axial direction introduced earlier employs a single Bessel argument α and a single response $\mathcal{L}_n(\tau)$. Three mathematically consistent mappings justify this compactification as:

(A) Dominant-drive approximation: When either z or z' dominates numerically (e.g. $z \gg z'$), we neglect the weaker term and set $\alpha \approx z$ (or z'). Then we have

$$S_{\rm harm}(\tau) \approx \sum_n J_n^2(\alpha)\,\mathcal{L}_n^{(\rm eff)}(\tau),$$

with $\mathcal{L}_n^{(\rm eff)}$ equal to the corresponding $\mathcal{L}_n^{(1)}$ or $\mathcal{L}_n^{(2)}$.

(B) Effective-weight identification: This define the coefficients c_1, c_2 (dependent on geometry) and an α such that, for a linear combination of the Bessel weight J_n^2 and response term $\mathcal{L}_n$ each n is,

$$J_n^2(\alpha)\,\mathcal{L}_n(\tau) \equiv c_1\,J_n^2(z')\,\mathcal{L}_n^{(1)}(\tau) + c_2\,J_n^2(z)\,\mathcal{L}_n^{(2)}(\tau).$$

Selecting $c_{1,2}$ and possibly α to match the low-order harmonics yields an effective single-sum representation for practical fitting.

(C) Exact single-sum representation: Formally we may define an effective pair $(\alpha, \mathcal{L}_n)$ as

$$J_n^2(\alpha)\,\mathcal{L}_n(\tau) \equiv J_n^2(z')\,\mathcal{L}_n^{(1)}(\tau) + J_n^2(z)\,\mathcal{L}_n^{(2)}(\tau), \tag{14}$$

which algebraically merges the two terms into one. With this definition,

$$S_{\rm harm}(\tau) = \sum_{n=-\infty}^{\infty} J_n^2(\alpha)\,\mathcal{L}_n(\tau). \tag{15}$$

Eq. (14) is simply a relabelling, and it does not loose the exact microphysics provided $\mathcal{L}_n(\tau)$ and α are permitted to be n-dependent objects or to be fitted functions.

To account phenomenologically for temperature-dependent dephasing and incoherent loss of harmonic weight, we multiply the spectral sum by $D(T)$ with $0 < D(T) \le 1$. Thus we define

$$S(T) \equiv \sum_{n=-\infty}^{\infty} J_n^2(\alpha)\,\mathcal{L}_n(\tau)\,D(T). \tag{16}$$

We therefore take the Lorentzian form $\mathcal{L}_n(\tau)$ commonly as:

$$\mathcal{L}_n(\tau) \equiv \frac{1}{1+\left(\omega - n\omega_B\right)^2\tau^2}, \tag{17}$$

where ω_B is the characteristic Bloch or band frequency appropriate to the miniband structure (it absorbs the Ω-type shifts from the microscopic denominators).

We further proceed to derive the thermal prefactor by evaluating the energy integral for the current in the non-degenerate limit. With reference to the linear-response, the acoustoelectric current density along z re-written as:

$$J_{AE} \;=\; e\int_{\vartheta_c}^{\infty} v_z(\vartheta)\,\tau(\vartheta)\,g(\vartheta)\,\mathcal{F}(\vartheta)\left[-\partial_\vartheta \mathcal{F}(\vartheta)\right]d\vartheta, \tag{18}$$

where $g(\vartheta)$ is the DOS (per unit length/volume), $\mathcal{F}(\vartheta)$ collects the drive/harmonic factors, i.e., Bessel weights and resonance denominators where $\mathcal{F}(\vartheta) = [1 + e^{(\vartheta-\varrho)/kT}]^{-1}$. Assuming a Maxwell–Boltzmann limit where the chemical potential satisfies $\varrho \ll \vartheta_c$, then

$$\mathcal{F}(\vartheta) = \exp\left[(\varrho - \vartheta)/kT\right], \qquad \text{and} \qquad -\partial_\vartheta \mathcal{F}(\vartheta) = \frac{1}{kT}\exp\left[(\varrho - \vartheta)/kT\right].$$

Now assume that $\mathcal{F}(\vartheta)$ varies slowly over the narrow energy window that dominates the integral, so $\mathcal{F}(\vartheta) \approx \mathcal{F}(\vartheta_c)$ and can be taken outside the integral. Then

$$J_{AE} = e\,\frac{\mathcal{F}(\vartheta_c)}{kT}\int_{\vartheta_c}^{\infty} v_z(\vartheta)\,\tau(\vartheta)\,g(\vartheta)\,\exp\left[(\varrho - \vartheta)/kT\right]d\vartheta. \tag{19}$$

For a slowly varying product near the band edge can be expanded as

$$v_z(\vartheta)\,\tau(\vartheta)\,g(\vartheta) \approx A\left(\frac{\vartheta - \vartheta_c}{\vartheta_0}\right)^{\beta}, \tag{20}$$

with constants $A, \vartheta_0 > 0$ and exponent $\beta \ge 0$ determined by DOS and velocity scalings (e.g., $\beta = 0$ for approximately constant product). Changing the variable $x \equiv (\vartheta - \vartheta_c)/kT$, then

$$\int_{\vartheta_c}^{\infty} (\vartheta - \vartheta_c)^{\beta} e^{-(\vartheta-\vartheta_c)/kT}\,d\vartheta = (kT)^{\beta+1}\,\Gamma(\beta+1).$$

Substituting into Eq. (19) yields

$$J_{AE} = e\,\mathcal{F}(\vartheta_c)\,A\,\vartheta_0^{-\beta}\,\Gamma(\beta+1)\,(k)^{\beta}\,T^{\beta}\,\frac{1}{T}\,\exp\!\left(\frac{\varrho - \vartheta_c}{kT}\right). \tag{21}$$

Hence the thermal prefactor scales as $T^{\beta-1}e^{(\varrho-\vartheta_c)/kT}$. Setting $\beta = 0 \Rightarrow T^{-1}$ prefactor i.e. $v_z\tau g$ approximately constant in the contributing window gives

$$J_{AE} \propto \frac{1}{T}\exp\!\left(\frac{\varrho - \vartheta_c}{kT}\right)\mathcal{F}(\vartheta_c).$$

We introduce a convenient reference temperature T_0 and absorb the constants into J_0, and explicitly factor the scattering normalisation τ/τ_0. This deduction yields the ansatz in the compact form as:

$$J_{AE}(T) \;=\; J_0\,\frac{T_0}{T}\exp\!\left(\frac{\varrho - \vartheta_c}{kT}\right)\frac{\tau}{\tau_0}\,S(T), \tag{22}$$

with $S(T)$ defined in Eq. (16) and J_0 embodies the geometry or material prefactor given as

$$J_0 = \frac{J_{0z}}{2} + \frac{J_{0s}}{2}\sin^2\vartheta. \tag{23}$$

We however deduce that, the microscopic harmonic sums; $\sum_n J_n^2(z')\mathcal{L}_n^{(1)} + J_n^2(z)\mathcal{L}_n^{(2)}$ are algebraically equivalent to a single sum $\sum_n J_n^2(\alpha)\mathcal{L}_n$ once the effective parameters α and $\mathcal{L}_n$ are allowed to encode both contributions (cf. Eq. (14)). Practically, we can choose (A), (B) or (C) depending on the desired accuracy we wish to obtain. The thermal factor $\frac{T_0}{T}\exp\left[(\varrho - \vartheta_c)/kT\right]$ follows from the non-degenerate limit and the assumption $\beta = 0$ where $v\tau g$ is constant near ϑ_c. If $\beta \neq 0$ the prefactor generalises to $T^{\beta-1}e^{(\varrho-\vartheta_c)/kT}$. The scattering-time dependence is displayed explicitly by factorising τ/τ_0, and the residual τ-dependence remains inside the Lorentzian term $\mathcal{L}_n(\tau)$.

Substituting the terms together yields

$$J_{AE} = J_0\,\frac{T_0}{T}\exp\!\left(\frac{\varrho - \vartheta_c}{kT}\right)\frac{\tau}{\tau_0}\sum_{n=-\infty}^{\infty} J_n^2(\alpha)\,\frac{1}{1+(\omega - n\omega_B)^2\tau^2}\,\mathcal{D}(T) \tag{24}$$

where

$$J_{os} = -\frac{e\Phi\Lambda^2 q^2\tau n_o d_s^2 d_z\theta(1-\alpha_s^2)\Delta_s^2\sin(2\ A)\sin(qd_s)}{4T\pi\hbar^2\rho v_s\omega_q\sin(qd_s/2)\sqrt{1-\alpha_s^2}\,I_o(\Delta_s/T)}$$

$$J_{oz} = -\frac{e\Phi\Lambda^2 q^2 \tau n_o d_s d_z^2 \theta(1-\alpha_z^2)\Delta_z^2 \sin(2\ A)\sin(qd_z)}{4T\pi\hbar^2 \rho v_s \omega_q \sin(qd_z/2)\sqrt{1-\alpha_z^2}\, I_o(\Delta_z/T)}.$$

2.2. Acoustoelectric conversion efficiency

The acoustoelectric conversion efficiency quantifies how effectively an acoustic wave can be converted into an electrical signal via carrier–phonon interaction in the FSWCNT system. It is, however, defined as the ratio of the output electrical power to the incident acoustic power delivered to the interaction region:

$$\eta = \frac{P_{\rm el}(T)}{P_{\rm ac,in}}. \tag{25}$$

Here, $P_{\rm el}(T)$ is the electrical power extracted at temperature T, while $P_{\rm ac,in}$ denotes the acoustic power supplied by the incident phonon flux. The ratio provides a dimensionless measure of how efficiently acoustic energy is transduced into electrical energy via the acoustoelectric effect.

Microscopic-to-macroscopic link: The acoustoelectric effect produces a measurable acoustoelectric current density $J_{\rm AE}(T)$ along the FSWCNT axis. Microscopically, this current originates from the momentum transfer between travelling acoustic phonons and conduction electrons. The phonon wave of frequency ω_q and wavevector q exerts a periodic perturbation on the carrier distribution function $F(\vartheta)$, which — after time averaging — gives rise to a net drift current proportional to the phonon flux.

Macroscopic electrical power is then extracted when this current flows across an effective electric field $\mathcal{E}_0$ developed along the FSWCNT length L. The instantaneous electrical power density (energy per unit volume per unit time) delivered to an external circuit is therefore

$$p_{\rm el}(T) = J_{\rm AE}(T)\,\mathcal{E}_0 \tag{26}$$

For a device with cross-sectional area $\mathcal{A}$ and length L, the total power is obtained by integrating this density over the interaction volume:

$$P_{\rm el}(T) = p_{\rm el}(T)\,\mathcal{A}L = J_{\rm AE}(T)\,\mathcal{E}_0\,\mathcal{A}\,L. \tag{27}$$

Acknowledging that $V = \mathcal{E}_0 L$ is the voltage drop and $I(T) = J_{\rm AE}(T)\mathcal{A}$ is the total acoustoelectric current, Eq. (27) simplifies to the familiar form

$$P_{\rm el}(T) = I(T)\,V = J_{\rm AE}(T)\,\mathcal{A}\,V. \tag{28}$$

Alternatively, the power per unit length is given by

$$\frac{P_{\rm el}(T)}{L} = J_{\rm AE}(T)\,\mathcal{E}_0\,\mathcal{A}.$$

This formalism is fully general and remains valid whether the system is considered in total power (W) or as power densities (W/m or W/m^2).

Acoustic energy input: The acoustic power incident on the FSWCNT is characterised by the acoustic intensity $\mathcal{I}_{\rm ac}$, which represents the phonon energy flux (W/m^2) across the cross-sectional area $\mathcal{A}$. Thus, the total acoustic power impinging on the interaction region is

$$P_{\rm ac,in} = \mathcal{I}_{\rm ac}\,\mathcal{A}. \tag{29}$$

On the microscopic scale, the acoustic flux intensity can be represented by the flow of phonon Φ, i.e., phonons per unit area per unit time and the phonon energy $\hbar\omega_q$ as:

$$\mathcal{I}_{\rm ac} = \Phi\,\hbar\omega_q \quad \Rightarrow \quad P_{\rm ac,in} = \Phi\,\hbar\omega_q\,\mathcal{A}. \tag{30}$$

This relation links the frequency spectrum and underlying phonon population to the macroscopic power flux. Thus, the scattering rate and phonon absorption probability, which are incorporated in the relaxation time τ, control the energy transfer between phonons and charge carriers.

Substituting Eqs. (28) and (29) into Eq. (25) gives

$$\eta = \frac{J_{\rm AE}\,V}{\mathcal{I}_{\rm ac}} = \frac{J_{\rm AE}\,\mathcal{E}_0}{\mathcal{I}_{\rm ac}} \quad (V = \mathcal{E}_0 L). \tag{31}$$

According to (31), the conversion efficiency is inversely correlated with the intensity of the incident acoustic field and directly correlated with the acoustoelectric current density. A stronger acoustoelectric current at a given acoustic intensity implies higher transduction efficiency.

Invoking the compact model for the acoustoelectric current derived earlier, we have

$$J_{\rm AE}(T) = J_0 \frac{T_0}{T}\,\exp\!\Big(\frac{\varrho-\vartheta_c}{kT}\Big)\,\frac{\tau}{\tau_0}\,S(T), \tag{32}$$

where J_0 is a prefactor representing the baseline current amplitude, and the factor

$$S(T) = \sum_{n=-\infty}^{\infty} J_n^2(\alpha)\,\mathcal{L}_n\,\mathcal{D}(T), \qquad \text{and} \qquad \mathcal{L}_n = \frac{1}{1+(\omega-n\omega_B)^2\tau^2}, \tag{33}$$

contains the entire harmonic and resonance structure of the acoustoelectric effect. Here, $\mathcal{D}(T) \le 1$ is a phenomenological damping factor that accounts for temperature-dependent dephasing or carrier scattering.

Substituting Eq. (32) into Eq. (31) yields

$$\eta = \frac{\mathcal{E}_0}{\mathcal{I}_{\rm ac}}\,J_0\,\frac{T_0}{T}\,\exp\!\Big(\frac{\varrho-\vartheta_c}{kT}\Big)\,\frac{\tau}{\tau_0}\,S(T). \tag{34}$$

Equivalently, since $V = \mathcal{E}_0 L$,

$$\eta = J_0\,\frac{V}{\mathcal{I}_{\rm ac}\,L}\,\frac{T_0}{T}\,\exp\!\Big(\frac{\varrho-\vartheta_c}{kT}\Big)\,\frac{\tau}{\tau_0}\,\mathcal{D}(T)\sum_{n=-\infty}^{\infty} J_n^2(\alpha)\,\frac{1}{1+(\omega-n\omega_B)^2\tau^2}. \tag{35}$$

Eqs. (34)–(35) are the final analytical expressions for the acoustoelectric conversion efficiency, incorporating thermal activation, scattering, harmonic response, and Bloch resonance physics. We now seek the origin and the physical interpretation of the parameters in Eq. (34) as follows:

- The term $\frac{\mathcal{E}_0}{\mathcal{I}_{\rm ac}}\,J_0$ connects the strength of the extraction field to the acoustic excitation. Increasing the dc electric field $\mathcal{E}_0$ linearly increases η until nonlinear scattering or heating arises.
- The term $\frac{T_0}{T}\exp[(\varrho-\vartheta_c)/kT]$ emerges from the Boltzmann kinetic equation, and this quantifies the carrier population available for phonon–electron coupling. This parameter encapsulates the thermal activation over the energy barrier $(\vartheta_c - \varrho)$.
- The parameter $\frac{\tau}{\tau_0}$ measures the degree of momentum relaxation, i.e., longer scattering times allow more coherent carrier drift and higher acoustoelectric efficiency.
- The harmonic sum $S(T)$ captures the nonlinear interaction between the ac drive and carrier motion in the FSWCNT. The Bessel terms $J_n^2(\alpha)$ describe sideband mixing, while $\mathcal{L}_n$ introduces Lorentzian-like resonances at integer multiples of the Bloch frequency, which reflect the dynamic localisation or miniband oscillation effects.
- Also, $\mathcal{D}(T)$ captures incoherent damping mechanisms (e.g., phonon–phonon scattering or impurity dephasing) that suppress the harmonic amplitudes at high temperature.

From Eq. (35), we observe several scaling and limiting behaviour trends which follow naturally as:

- *Linear field dependence:* $\eta \propto \mathcal{E}_0$ or $\propto V$ for moderate fields; higher fields increase extracted electrical power until nonlinearities emerge.
- *Thermal response:* The thermal prefactor increases with temperature in the nondegenerate regime ($\varrho < \vartheta_c$), which enhances η up to an optimal temperature T^*, beyond which damping dominates.
- *Resonant enhancement:* When the ac frequency ω approaches $n\omega_B$, the denominator of $\mathcal{L}_n$ minimises, which produces peaks in $S(T)$ and thus resonant enhancement of η.

- *Efficiency bound:* Physical conservation demands $0 < \eta \leq 1$; practical efficiencies in FSWCNT-based acoustoelectric devices typically range between 10^{-6} and 10^{-2}.
- *Crossover behaviour:* If $D(T)$ decreases rapidly beyond a characteristic temperature, $\eta(T)$ is suppressed even as the thermal prefactor is enhanced, marking the onset of dephasing or miniband leakage.

Eqs. (31) and (35) present a compact yet comprehensive form of the acoustoelectric conversion efficiency. The model shows that efficient acoustoelectric conversion in FSWCNTs requires (i) strong acoustic coupling (large I_{ac}), (ii) optimal carrier relaxation times, (iii) resonance tuning between ω and ω_B, and (iv) moderate operating temperatures minimising damping. Together, these determine the achievable range of $\eta(T)$ and the conditions for practical acoustoelectric transduction.

2.3. Validity of the semiclassical Boltzmann transport equation

The semiclassical BTE has been widely employed to investigate carrier transport in low-dimensional materials whenever the electronic band structure is treated quantum mechanically while the carrier dynamics are described statistically [28,30,31]. Although SWCNTs are intrinsically quantum-confined systems, the use of the BTE remains appropriate provided that the dominant transport mechanism is incoherent scattering rather than coherent wave propagation. The carrier dynamics are governed by Eq. (32).

An important feature of the present formulation is that the quantum nature of the nanotube is not neglected. Instead, quantum confinement enters through the tight-binding electronic dispersion relation, which incorporates the effects of circumferential quantisation and the resulting one-dimensional electronic subbands that exhibit van Hove singularities.

Consequently, the BTE describes the evolution of electrons within quantum subbands rather than free electrons in a classical conductor. The validity of the semiclassical approximation depends upon the relationship between the electron mean free path, $\ell = v_{\mathrm{F}}\tau$, the phase coherence length, L_ϕ, and the characteristic transport length of the device. At elevated temperatures, electron–phonon scattering reduces the phase coherence length according to $L_\phi \propto T^{-p}$, where the exponent p depends upon the dominant scattering mechanism. Consequently, increasing temperature progressively suppresses coherent quantum transport while enhancing diffusive transport.

The temperature interval investigated in the present work ($100 \leq T \leq 500$ K) corresponds to thermal energies $k_{\mathrm{B}}T = 8.617 \times 10^{-5}T$ eV, yielding $k_{\mathrm{B}}T = 8.6$ meV(100 K) and $k_{\mathrm{B}}T = 43.1$ meV(500 K). These thermal energies are sufficiently large to broaden the carrier distribution around the Fermi level and promote frequent phonon-assisted scattering events. Under these conditions, transport is governed primarily by the statistical redistribution of carriers rather than by coherent wave interference.

Quantum tunnelling has also been neglected in the present analysis. This approximation is justified because tunnelling becomes dominant only when the transport length approaches a few nanometres or when resonant quantum states are established. Neither of these conditions applies to the present device geometry.

Likewise, transport through higher electronic subbands has not been considered. Since the carrier energies remain close to the lowest conduction subband under the investigated operating conditions, intraband transport dominates the electron dynamics. Inclusion of higher subbands would introduce only minor quantitative corrections without altering the principal trends reported in this work.

Accordingly, the present model combines a quantum mechanical description of the electronic structure with a semiclassical description of carrier transport. This mixed quantum–semiclassical approach has been widely adopted in the literature for finite-temperature transport in carbon nanotubes and provides an appropriate balance between physical accuracy and analytical tractability.

3. Results and discussion

The analytical expressions derived for the acoustoelectric current density and conversion efficiency η were evaluated numerically to examine their dependence on key physical parameters of the FSWCNT system. The results reveal a complex interplay between the applied dc field, the ac modulation, temperature, and scattering mechanisms in the FSWCNT. Analytical expressions describing the acoustoelectric conversion efficiency in FSWCNTs specifically, along the axial direction are derived and numerically evaluated using key parameters: $\omega_q = 10^{11}$ s^{-1}, $v_s = 2.5\times10^3$ m/s, $\Phi = 10^5$ Wb/m^2, $q = 10^6$ cm^{-1}, $\lambda = 10^{-5}cm^{-1}$ and $\ell = 10^{-4}$ cm.

The numerical calculations presented in this work employ experimentally accessible operating voltages. For a nanotube length of approximately 200 nm, the applied dc voltage is restricted to values below about 2 V, corresponding to electric fields that are routinely achieved in carbon nanotube transport experiments. Higher bias values shown in earlier versions of this work have been removed since they represent only theoretical extrapolations of the nonlinear model.

Fig. 2 illustrates the dependence of the (a) acoustoelectric efficiency (η) on voltage (V) for different values of acoustic intensities (I_{ac}); (b) Semilog plot (η) dependence on voltage (V) for different values of acoustic intensities (I_{ac}); (c) Dependence of acoustoelectric efficiency (η) on voltage (V) for different values of temperature; (d) Semilog (η) on voltage (V) for different values of temperature T; for $n_0 = 10^{19}$ cm^{-3}, $\Delta_s = 0.25$ eV and $\Delta_z = 0.25$ eV. Each panel 2(a–d) captures distinct aspects of the interaction between hot carriers induced by the ac or laser field and acoustic phonons in the FSWCNT system.

In Fig. 2(a), we observe that the efficiency η increases almost linearly with the applied voltage V (or equivalently, the dc electric field $\mathcal{E}_0$) at $T = 300$ K (see Fig. 2a). This behaviour follows directly from the theoretical relation obtained in Eq. (35). It is evident from the figure that at low and moderate fields, J_{AE} dependence on $\mathcal{E}_0$ varies only weakly, giving a quasi-linear rise of η with voltage. This observed trend corresponds to the Ohmic regime, where the carrier drift velocity scales linearly with the applied field and the carrier scattering is field-independent.

As $\mathcal{E}_0$ is enhanced, the Bloch frequency (ω_B) then approaches the ac drive frequency ω, which leads to a resonant enhancement through the Lorentzian term. At resonance, $\omega \approx n\omega_B$, and the denominator in $\mathcal{L}_n$ is minimised, producing sharp and enhanced peaks in η corresponding to efficient electron–phonon momentum transfer. Physically, these peaks signify synchronisation between Bloch oscillations and the ac field, yielding maximal energy conversion. Beyond this regime, excessive heating increases the carrier scattering and which slightly suppresses η.

We present in Fig. 2(b) the semilogarithmic variation of η with acoustic intensity I_{ac} at $T = 300$ K. The figure reveals a monotonic decline of η as I_{ac} increases, since the efficiency is inversely proportional to I_{ac}, as expressed in Eq. (35). As J_{AE} rises only moderately with I_{ac}, the denominator dominates, leading to a logarithmic decay in the semilog plot. At higher acoustic intensities, the strong phonon flux enhances carrier–phonon scattering, which shortens the relaxation time τ and this broadens the response function $\mathcal{L}_n$. This suppresses coherent electron–phonon coupling, which also suppresses η. The observed behaviour indicates a saturation regime, where increasing the acoustic power no longer contributes to effective energy conversion but instead increases dissipative losses through phonon heating caused by the laser field and inelastic scattering.

The variation of η with temperature is displayed in Fig. 2(c), which exhibits a non-monotonic behaviour—rising initially, peaking at an intermediate temperature T^*, and then decreasing at higher temperature values. This behaviour arises as a result of the competition between the thermal and scattering effects inherent in Eq. (16), where $S(T)$ denotes the harmonic summation. The term $\frac{T_0}{T}\exp[(\varrho - \vartheta_c)/(kT)]$ increases with temperature as more carriers are thermally excited

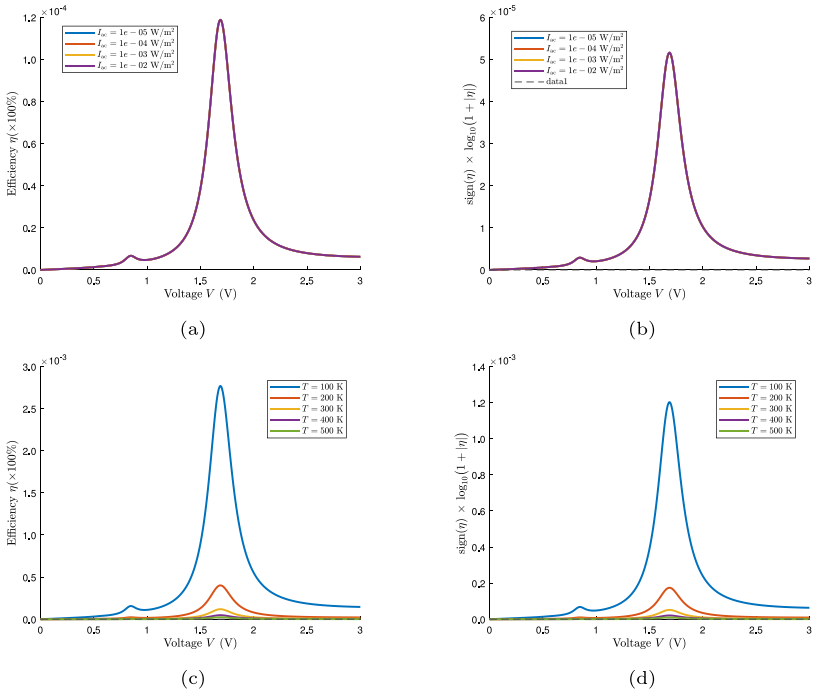


Fig. 2. (a) Dependence of acoustoelectric efficiency (η) on voltage (V) for different values of acoustic intensities (I_{ac}); (b) Semilog plot (η) dependence on voltage (V) for different values of acoustic intensities (I_{ac}); (c) Dependence of acoustoelectric efficiency (η) on voltage (V) for different values of temperature; (d) Semilog (η) on voltage (V) for different values of temperature T.

above the band edge, thus enhancing the acoustoelectric current via intraminiband transition. However, as the temperature further increases, phonon–phonon and electron–phonon interactions become more and more intense, which reduces τ and introduces additional damping via $D(T)$. The efficiency therefore reaches a maximum at the temperature T^* where carrier activation and damping losses balance. For $T > T^*$, the increasing inelastic scattering and thermal dephasing dominate, leading to a decay in η. This peak marks the optimal operating temperature for efficient acoustoelectric energy conversion.

In Fig. 2(d), we show the semilog dependence of η on the applied dc voltage V for different temperature values. The semilog plot in this case is particularly useful in revealing the exponential nature of $\eta(V)$ variations that are not easily visible on a linear scale. At low voltages, η increases almost linearly, indicating that the hot carrier drift and acoustic wave coupling remain in the linear response regime. As V increases further, η rises sharply before reaching a saturation region where additional voltage produces diminishing returns. This behaviour signifies the onset of nonlinear carrier dynamics and the partial breakdown of coherence between the electronic and acoustic subsystems.

The influence of temperature is also clearly evident because high temperatures lower the magnitude of η across all voltages systematically. This occurs because the elevated thermal energy increases electron–phonon scattering, and this shortens the relaxation time τ, and broadens the carrier energy distribution, thus suppressing coherent momentum transfer. Conversely, at low temperatures, reduced phonon activity allows electrons to interact more resonantly with the acoustic field, which results in high efficiency and a more pronounced voltage-dependent growth.

The nearly exponential slope of the semilog curves at moderate voltages suggests that η follows an approximate relation of the form

$$\eta(V,T) \propto \exp[-\gamma(T)/V], \tag{36}$$

where $\gamma(T)$ is a temperature-dependent coefficient reflecting the strength of dissipative scattering processes. The intersection of the curves at high voltages implies a universal behaviour where the effect of temperature becomes less dominant once the field-driven carrier acceleration surpasses thermal broadening effects. Thus, the figure demonstrates that both voltage and temperature play competing roles; increasing V enhances carrier energy and promotes efficient acoustoelectric conversion, whilst higher temperature introduces scattering that weakens coherence. The semilog trend thus captures the delicate balance between field-driven transport and thermal damping that controls η in F–SWCNT.

Fig. 3 shows the dependence of (a) acoustoelectric efficiency (η) on voltage (V) for different values of Δ_s; (b) Semilog plot (η) on voltage (V) for different values of Δ_s; (c) acoustoelectric efficiency (η) on voltage (V) for different values Δ_z; (d) Semilog (η) on voltage (V) for different values of Δ_z.

The figure describes the influence of the microscopic geometric parameters — specifically the overlap integrals Δ_s and Δ_z — and the chiral configuration of the F–SWCNT on the conversion efficiency, η. These parameters enter the theoretical model through the current prefactor J_0 and determine how strongly electrons couple to the applied fields along the circumferential and axial directions of the F–SWCNT.

Fig. 3(a) shows that the conversion efficiency η varies noticeably with the circumferential overlap integral Δ_s. In the Huckel–matrix framework, Δ_s represents the probability amplitude for carrier hopping between adjacent carbon atoms along the circumferential direction of the F–SWCNT. This parameter regulates the transverse quantisation of the electronic states and the degree of subband mixing between different angular momentum channels. Increasing Δ_s broadens the electronic bandwidth around the circumference and modifies the effective density of states involved in electron–phonon interactions. Since J_{AE} is proportional to the gradient of the electronic band energy with respect to the wavevector, Δ_s enters through the term

$$J_0 \propto e n_0 \Delta_s d_s \sin\left(\frac{p_s d_s}{\hbar}\right), \tag{37}$$

which multiplies the temperature- and field-dependent factors. For small Δ_s, the electronic states are more localised along the tube axis, resulting in stronger longitudinal coherence and high η values. As Δ_s

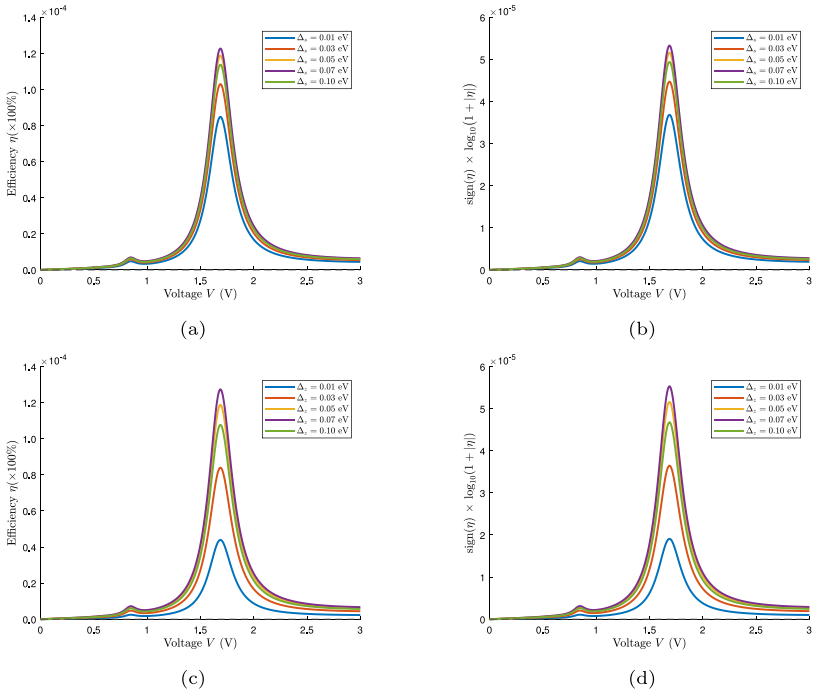


Fig. 3. (a) Dependence of acoustoelectric efficiency (η) on voltage (V) for different values of Δ_s; (b) Semilog plot (η) dependence on voltage (V) for different values of Δ_s; (c) Dependence of acoustoelectric efficiency (η) on voltage (V) for different values Δ_z; (d) Semilog (η) on voltage (V) for different values of Δ_z.

increases, enhanced transverse delocalisation and subband coupling introduce additional scattering channels that reduce the net longitudinal momentum transfer.

Physically, this behaviour implies that the circumferential coupling controlled by Δ_s modulates the balance between coherent axial transport and transverse band mixing. Optimal acoustoelectric performance is achieved when Δ_s is sufficiently small to preserve a one-dimensional transport while still allowing effective interatomic overlap for electron mobility.

Fig. 3(b) shows the semilog variation of η with applied voltage V for different values of the circumferential overlap integral Δ_s. The overlap integral Δ_s characterises the degree of electron hopping between neighbouring carbon atoms along the circumferential direction of the F–SWCNT and directly influences the electronic band structure and density of states. Variations in Δ_s therefore modify the transverse coupling between subbands and affect how effectively electrons exchange momentum with the propagating acoustic wave.

The semilog plot reveals that η increases exponentially with V at low voltages and gradually approaches a saturation regime at higher voltages. However, the slope and magnitude of $\eta(V)$ strongly depend on Δ_s. For small values of Δ_s, the curves exhibit a sharper exponential rise, which indicates a strong localisation of electronic states and enhanced electron–phonon coupling efficiency along the axial direction. Interband mixing intensifies with increasing Δ_s, resulting in increased dispersion in the circumferential direction and a decrease in the net longitudinal component of the carrier velocity.

Consequently, the efficiency decreases and the semilog curves flatten. This behaviour can be described approximately by

$$\eta(V, \Delta_s) \propto \exp\left[-\frac{\Gamma(\Delta_s)}{V}\right], \tag{38}$$

where $\Gamma(\Delta_s)$ is an effective scattering parameter that increases with Δ_s. Physically, a larger Δ_s enhances electron delocalisation and weakens the phase coherence necessary for efficient electron–phonon momentum exchange. At sufficiently high voltages, the field-induced acceleration of carriers dominates over the influence of Δ_s, and the curves converge, signifying that the system approaches a field-saturated regime in which the overlap integral plays a lesser role.

Therefore, we observe that Δ_s acts as a tuning parameter regulating the degree of band mixing and coherence in fluorine-doped SWCNTs, as observed in by the semilog plot (see Fig. 3(b)). Lower values of Δ_s favour strong longitudinal electron–phonon coupling and higher acoustoelectric efficiency, whilst larger values of Δ_s suppress η as a result of the enhanced transverse electron dispersion and increased inelastic scattering.

Fig. 3(c) shows that η increases significantly with the axial overlap integral Δ_z. In the Huckel-matrix description of electronic motion in F–SWCNTs, Δ_z quantifies the probability amplitude for electron hopping between adjacent sites along the F–SWCNT axis. The current density is proportional to the derivative of the band energy with respect to the wavevector, which scales with Δ_z. Thus, a higher Δ_z increases the electron–phonon coupling strength and the carrier velocity, which results in a bigger η and a higher J_{AE}. The prefactor

$$J_0 \propto e n_0 \Delta_z d_z \sin\left(\frac{p_z d_z}{\hbar}\right), \tag{39}$$

which multiplies the thermal and harmonic factors in Eq. (35), shows how Δ_z enters mathematically. Physically, this behaviour suggests that a higher overall conversion efficiency is achieved by facilitating longitudinal momentum transfer between electrons and acoustic phonons through increased π-orbital overlap along the tube axis.

For various values of the axial overlap integral Δ_z, Fig. 3(d) shows the semilogarithmic dependency of the conversion efficiency η on the applied dc voltage V. The longitudinal electronic-phonon coupling that controls charge transport is directly determined by Δ_z, which denotes the electron hopping energy between neighbouring atomic sites along the F–SWCNT axis. Changes in Δ_z alter the charge carrier's effective bandwidth and group velocity, which in turn affects the strength of the electron–phonon interactions that produce the acoustoelectric effect.

The semilog plot reveals that η increases exponentially with V at low bias and approaches saturation at higher voltages, consistent with field-induced acceleration of carriers followed by scattering-limited transport. However, the magnitude and slope of $\eta(V)$ depend strongly on Δ_z. The acoustoelectric efficiency is remarkably high, and the exponential rise with voltage is steeper for large Δ_z. This suggests that more

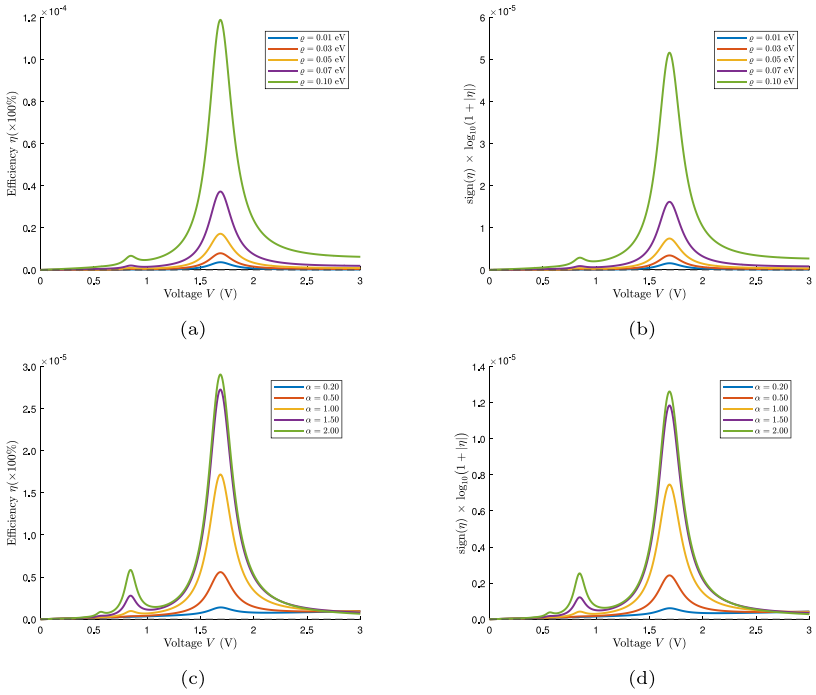


Fig. 4. (a) Dependence of acoustoelectric efficiency (η) on voltage (V) for different values of ϱ; (b) Semilog plot (η) dependence on voltage (V) for different values of ϱ; (c) Dependence of acoustoelectric efficiency (η) on voltage (V) for different values ac amplitude α; (d) Semilog (η) on voltage (V) for different values of ac amplitude α.

effective momentum transfer between the electrons and the acoustic wave is made possible by enhanced longitudinal electron–phonon coupling, which also enhances the carrier mobility.

On the contrary, the conduction channel narrows and becomes less coherent when Δ_z is tiny, which leads to a smoother semilog slope and a smaller η. The behaviour can be described approximately by

$$\eta(V, \Delta_z) \propto \exp\left[-\frac{\Gamma(\Delta_z)}{V}\right], \tag{40}$$

where $\Gamma(\Delta_z)$ is an effective damping factor that decreases as Δ_z rises, can be used to characterise the behaviour. For large Δ_z, the lowering of $\Gamma(\Delta_z)$ indicates longer carrier relaxation durations and moderate scattering, which is compatible with strong longitudinal delocalisation. The behaviour of the curves tends to merge at higher voltages, which shows that the system eventually saturates as the applied field overcomes the band-structure effects. The Δ_z is a crucial parameter in determining the η in FSWCNT, as the figure illustrates (see Fig. 3d). Increasing Δ_z strengthens axial electronic coherence, facilitates resonant energy transfer from the acoustic wave to the charge carriers, and thereby maximises η. These findings underscore the importance of optimising Δ_z—through control of tube chirality, strain, or interatomic spacing—to achieve superior acoustoelectric performance in F–SWCNT-based nanoscale devices.

Thus, Fig. 3(a–d) establish that the microscopic bonding parameters and the chiral structure of the FSWCNT critically determine the magnitude of the acoustoelectric conversion efficiency. Larger overlap integrals Δ_z and Δ_s improve electron delocalisation and enhance field coupling, but their effectiveness depends strongly on temperature and damping conditions. Chirality controls the degree of axial–circumferential coupling, thus influencing how effectively electrons respond to both dc and ac fields. The results confirm that optimising F–SWCNT geometry at the atomic scale — by tailoring Δ_z, Δ_s, and the chiral vector — is an essential pathway for achieving higher acoustoelectric conversion efficiency in nanoscale devices.

We display in Fig. 4 the dependence of (a) acoustoelectric efficiency (η) on voltage (V) for different values of ϱ; (b) Semilog plot (η) on voltage (V) for different values of ϱ; (c) acoustoelectric efficiency (η) on voltage (V) for different values ac amplitude α; and (d) Semilog (η) on voltage (V) for different values of ac amplitude α

The figure explores the influence of the ac field amplitude α, the drive frequency ω, and the resulting nonlinear electron–phonon interactions on the conversion efficiency η. The figure demonstrates how modulation of the ac component of the total electric field modifies the harmonic summation term, and consequently changes the magnitude and structure of η. The Bessel functions $J_n(\alpha)$ describe multiphoton sideband processes, while the Lorentzian term $\mathcal{L}_n$ accounts for resonant coupling between the drive frequency ω and the Bloch frequency. Each panel of Fig. 4 reveals a distinct regime of ac–dc field interaction.

In Fig. 4(a), the efficiency exhibits oscillatory dependence on α. This behaviour arises from the Bessel function weights $J_n^2(\alpha)$ in Eq. (35). For small α, only the fundamental harmonic ($n = 0$) contributes significantly, and η increases as α^2 due to the enhancement of the electron oscillation amplitude. As α increases, higher-order terms ($n = \pm 1, \pm 2, \ldots$) gain more weight and redistribute energy among multiple sidebands. The interference among these harmonics leads to constructive and destructive contributions to $S(T)$, resulting in oscillations of η with α.

Physically, these oscillations reflect the transition from the linear to the nonlinear regime of electron motion under combined ac–dc driving. At moderate α, the system exhibits photon-assisted transport, where electrons absorb or emit multiple photons of energy $\hbar\omega$ while interacting with acoustic phonons. At very high α, sideband saturation occurs, and the net efficiency decreases as phase mixing reduces coherent momentum transfer. The behaviour in Fig. 4(a) therefore demonstrates the nonlinear control of acoustoelectric conversion via field amplitude modulation.

Fig. 4(b) shows the semilog dependence of η on the applied dc voltage V for different values of the chemical potential ϱ. The chemical potential determines the Fermi level position and hence the number of electrons participating in transport and their average energy relative to the conduction subbands. In the Boltzmann transport framework, the ϱ term determines the occupation probability of electronic states that contribute to the J_{AE} acoustoelectric current density. This term is

accessed through the Fermi-Dirac term. Therefore, variations in ϱ adjust the total coupling strength between the electrons and the acoustic phonons and tailor the carrier population.

At low dc bias, η dependence on V rises exponentially. At high voltages, η tends to saturate, as observed in the figure (see Fig. 4b). The semilog slope steepens and the magnitude of η increases as ϱ rises, which suggests a greater acoustoelectric connection. More carriers that can exchange momentum via intraminiband transition with the acoustic field result from a higher density of occupied states close to the Fermi level, which is caused by a higher chemical potential. However, when ϱ becomes very large, degeneracy effects and Fermi screening reduce the modulation of carrier distribution by the acoustic wave, leading to a slower growth and eventual saturation of η.

The behaviour can be approximated by

$$\eta(V,\varrho) \propto \varrho \exp\left[-\frac{\Gamma(\varrho)}{V}\right], \tag{41}$$

where $\Gamma(\varrho)$ is an effective damping parameter that increases slowly with ϱ as electron–electron interactions and screening effects become significant. The semilog dependence indicates that the rate of exponential growth of η with V is controlled by the relative position of the Fermi level: low ϱ (non-degenerate regime) yields weak coupling and small η, while high ϱ (degenerate regime) enhances the coherent electron–phonon interaction up to a saturation limit.

Thus, Fig. 4(b) demonstrates the dependency of η on the applied voltage for different values of chemical potential ϱ for $T = 300$ K, $n_0 = 10^{19}$ cm^{-3}, $\Delta_z = 0.25$ eV, acting as a key tuning parameter of the acoustoelectric efficiency. Increasing ϱ enhances η by filling higher-energy electronic states and strengthening the electron–phonon interaction; however, excessive Fermi-level elevation results in screening and degeneracy that limit additional improvement. Optimal performance is therefore achieved at moderate ϱ, where carrier density and coherence are both maximised for efficient acoustoelectric conversion in carbon nanotubes.

Fig. 4(c) demonstrates the combined variation of η with α at different driving frequencies ω. The efficiency oscillates with α, but both the amplitude and position of these oscillations shift as ω changes. This interplay arises because the Bessel factors $J_n^2(\alpha)$ and the Lorentzian terms $\mathcal{L}_n$ jointly determine the harmonic content of $S(T)$. The Lorentzian factor amplifies η at frequencies near ω_B by significantly enhancing the contribution of a certain n harmonic. $\mathcal{L}_n$ broadens and the contributions from various harmonics overlap as ω moves away from resonance, flattening the oscillations.

Mathematically, $\eta(\alpha,\omega)$ can be approximated by retaining only the dominant harmonic term:

$$\eta(\alpha,\omega) \approx C J_n^2(\alpha) \frac{1}{1+(\omega - n\omega_B)^2\tau^2}, \tag{42}$$

where C is a constant containing temperature and damping factors. This expression captures the shifting maxima observed in the figure (see Fig. 4c). Physically, the variation highlights that the efficiency can be dynamically tuned through simultaneous modulation of both field amplitude and frequency—a key feature for device applications such as field-controlled acoustoelectric amplifiers.

The semilogarithmic relationship between the applied dc voltage V and the acoustoelectric conversion efficiency η for varying ac field amplitudes α is shown in Fig. 4(d). The strength of the alternating electric field corresponding to photon energy is measured by the ac amplitude $\alpha = e\mathcal{E}_1 d/(\hbar\omega)$, which measures the degree of nonlinear modulation in the carrier dynamics.

The system functions in the linear-response regime at low α, where the fundamental harmonic ($n = 0$) dominates the Bessel function expansion of the electron distribution, causing η to grow nearly exponentially with V. Higher-order sidebands ($n \neq 0$) start to make a substantial contribution as α rises owing to the $J_n^2(\alpha)$ weighting in the spectral summation, which controls the overall field dependence of η. This redistribution of spectral weight among multiple harmonics modifies the effective coupling strength and phase coherence of the electron–phonon interaction.

The semilog plot shows that as α increases, the exponential growth of η with V becomes less steep, and the efficiency curves shift downward. This indicates that strong ac modulation induces multiphoton processes that broaden the resonance between the Bloch frequency ω_B and the ac drive ω, thereby reducing the net coherent transfer of energy from the acoustic field to the electronic subsystem. The efficiency in this regime can be approximated by

$$\eta(V,\alpha) \propto \mathcal{M}(\alpha) \exp\left[-\frac{\Gamma(\alpha)}{V}\right], \tag{43}$$

where $\mathcal{M}(\alpha)$ represents the α-dependent harmonic weight and $\Gamma(\alpha)$ is an effective damping parameter that increases with α as sideband mixing and inelastic scattering intensify.

At moderate α, resonant enhancement may occur when one of the Bessel-weighted sidebands aligns with $\omega_B \approx n\omega$, leading to local peaks or inflections in the semilog traces. However, at large α, the spectrum becomes overbroadened, causing destructive interference among harmonics and saturation of η at high voltages. This saturation signifies the limit of coherent acoustoelectric energy transfer under strong-field conditions.

Fig. 4(d) demonstrates that the ac amplitude α serves as a powerful control parameter for tuning the nonlinear acoustoelectric response. Small α favours sharp, resonant growth of η with voltage, while large α introduces multiphoton sideband interactions that suppress efficiency. Optimising α within an intermediate range therefore maximises the field-driven coupling between acoustic and electronic modes in carbon nanotubes.

However, Fig. 4(a–d) confirm that the acoustoelectric conversion process in FSWCNTs is inherently nonlinear and highly sensitive to the parameters of the ac field. The oscillatory behaviour with respect to α, the resonant enhancement at $\omega \approx \omega_B$, and the temperature-dependent saturation at strong fields collectively indicate that η can be dynamically controlled through external field parameters. These observations illustrate the potential of FSWCNT-based acoustoelectric systems as tunable nanoscale energy converters, in which the frequency and amplitude of applied electromagnetic fields may be regulated to tailor the coupling between hot carriers and acoustic phonons.

In Fig. 5(a), η exhibits distinct resonant peaks as ω_B increases. This behaviour follows from the Lorentzian form of the harmonic response function, which appears in the summation term $S(T)$. The efficiency reaches its maximum when $\omega \approx n\omega_B$, corresponding to the resonance between the applied ac drive and the natural Bloch oscillation frequency of electrons in the FSWCNT's periodic potential. At resonance, there is a significant connection between the electronic and acoustic systems and a noticeable amplification of η as the electron motion synchronises with the field oscillations.

The response is dominated by the primary peak ($n = 1$) of the Bloch oscillation, while each resonance peak represents a harmonic (nth order). As ω_B rises further, higher-order harmonics ($n = 2, 3, \ldots$) appear, but their amplitudes are smaller due to a drop in the Bessel weights $J_n^2(\alpha)$. Physically, this pattern indicates that the acoustoelectric effect in FSWCNTs is governed by a hierarchy of field-induced resonances, analogous to the harmonic response observed in semiconductor superlattices.

The semilog (η) dependence on the applied voltage V for different values of Bloch frequency ω_B for $T = 300$ K, $n_0 = 10^{19}$ cm^{-3} and $\Delta_z = 0.25$ eV is displayed in Fig. 5b (see Fig. 5b), which illustrates the characteristic frequency of the electron oscillations in the period potential of the fluorine-doped SWCNT under a constant dc electric field. The semilog representation makes the impact of ω_B on the rate of growth and saturation more noticeable and emphasises the exponential dependency of η on V.

For low ω_B, which is equivalent to lower dc bias fields, the electrons undergo delayed Bloch oscillations with reduced kinetic energy. This

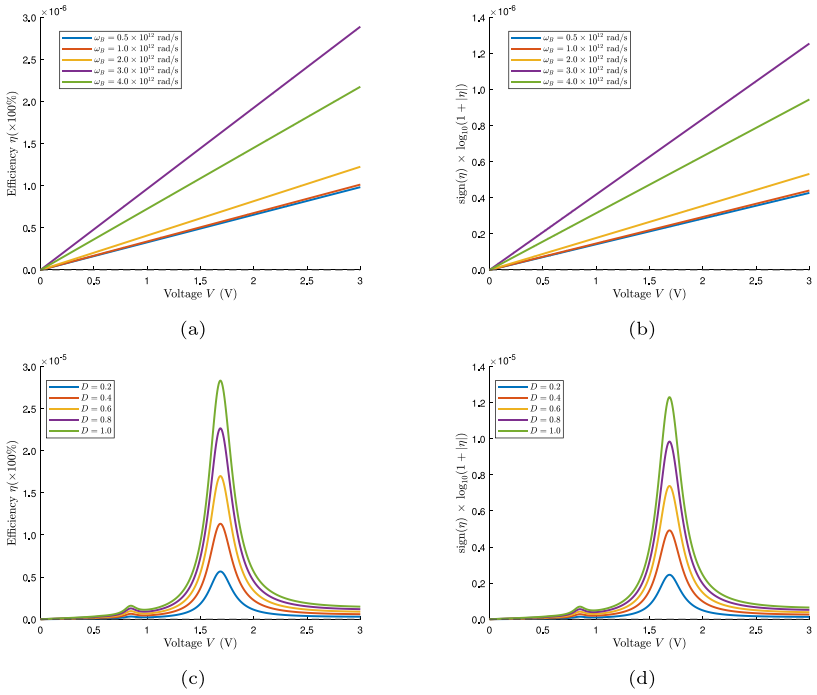


Fig. 5. (a) Dependence of acoustoelectric efficiency (η) on voltage (V) for different values of ω_B; (b) Semilog plot (η) dependence on voltage (V) for different values of ω_B; (c) Dependence of acoustoelectric efficiency (η) on voltage (V) for different values damping factor D; (d) Semilog (η) on voltage (V) for different values of damping factor D.

phenomenon leads to a mild exponential slope and a comparatively tiny η. By strengthening the connection between the electrons and the acoustic wave, ω_B increases the rate of coherent electron oscillations. The $\eta(V)$ curves show more effective energy transfer from the acoustic to the electrical subsystem since they rise upward and have a larger semilog slope. This behaviour persists until ω_B approaches the ac drive frequency ω, at which point resonance conditions are satisfied and η reaches its maximum value.

The behaviour of the figure also reveals that beyond the resonance condition ($\omega_B > \omega$), the growth of η with voltage begins to saturate and may even decline slightly. This occurs because excessively high ω_B drives electrons too rapidly through the Brillouin zone, reducing their ability to remain in phase with the acoustic field. The efficiency in this regime can be described approximately by

$$\eta(V, \omega_B) \propto \mathcal{N}(\omega_B) \exp\left[-\frac{\Gamma(\omega_B)}{V}\right], \tag{44}$$

where $\mathcal{N}(\omega_B)$ represents the resonance amplitude that peaks near $\omega_B \approx n\omega$, and $\Gamma(\omega_B)$ is an effective damping factor that increases once the oscillation frequency exceeds the phonon response time.

The trend displayed in Fig. 5(b) physically shows how the Bloch frequency functions as a controllable measure of the strength of the interaction between the acoustic and electrical modes. After resonance, scattering and phase mismatch take over, which leads to an exponential attenuation in the semilog plot (see Fig. 5b). Initially, increasing ω_B enhances coherence and increases η. The curves' convergence at high V, which depicts a change to a field-saturated domain where additional efficiency increases are constrained by pronounced nonlinear effects.

The figure, however, underscores the relevance of Bloch frequency in determining the acoustoelectric's performance. Accurately tuning ω_B to match the ac driving frequency permits resonant amplification of η. Any variation from this condition leads to exponential suppression, underlining the significant role of field control in optimising FSWCNT-based acoustoelectric systems.

In Fig. 5c we demonstrate the acoustoelectric efficiency η dependence on the applied dc voltage V for different values of the damping factor $D(T)$, for $T = 300$ K, $n_0 = 10^{19}$ cm^{-3} and $\Delta_z = 0.25$ eV is displayed in Fig. 5c (see Fig. 5 c). The damping factor encapsulates all dissipative mechanisms — primarily electron–phonon scattering, phonon–phonon interactions, impurity scattering, and lattice imperfections — that degrade the coherence of carrier motion in the nanotube. In the theoretical model, $D(T)$ appears as a multiplicative attenuation term in the spectral function $S(T)$, such that increasing $D(T)$ directly weakens the amplitude of both the current density J_{AE} and the overall efficiency η.

The plot shows that for all damping values, η initially increases with V as the applied field accelerates charge carriers and enhances electron–phonon coupling. However, as $D(T)$ increases, both the magnitude of η and the steepness of its voltage dependence decrease significantly. This behaviour indicates that higher damping suppresses the resonant transfer of energy between the acoustic wave and the electron subsystem by reducing the effective relaxation time τ and disturbing the phase coherence required for Bloch oscillations. In the low-damping limit ($D(T) \to 0$), the electrons maintain long coherence times, resulting in a strong, nearly quadratic dependence of η on V. Conversely, for a high-damping regime, $\eta(V)$ becomes sublinear, which reflects dominance of the diffusive transport by random scattering events.

This effect can be approximated as

$$\eta(V, D) \approx \frac{\mathcal{A}}{1 + \beta D}\left[1 - \exp\left(-\frac{V}{V_0}\right)\right], \tag{45}$$

where $\mathcal{A}$ represents the maximum attainable efficiency at vanishing damping, β is a proportionality constant related to the strength of scattering, and V_0 is a characteristic saturation voltage. As D increases, the prefactor $\mathcal{A}/(1 + \beta D)$ decreases, producing lower overall η values and weaker field dependence.

Physically, Fig. 5(c) demonstrates that the damping factor D is a critical control parameter that determines the balance between coherent and incoherent transport in the acoustoelectric process. Small D values correspond to high-purity, low-defect nanotubes with long relaxation times, which favour strong electron–phonon coupling and large η. In contrast, large D values — arising from phonon scattering,

impurity defects, or thermal disorder — introduce energy losses that convert a substantial fraction of the acoustic input into heat rather than electrical power. The behaviour observed underscores the necessity of minimising damping to achieve high-efficiency acoustoelectric energy conversion in FSWCNT–based nanodevices.

We present in Fig. 5(d) the semilog dependence of the acoustoelectric conversion efficiency η on the applied voltage V for various values of the damping factor D. The damping factor encapsulates the total energy dissipation in the system arising from electron–phonon scattering, lattice imperfections, and other inelastic processes. In the theoretical framework adopted, D enters as a multiplicative attenuation term in the spectral function, thereby directly modulating the amplitude of the acoustoelectric response. The semilog representation clearly exposes the exponential sensitivity of η to variations in both V and D.

At small D values (weak damping), we observe a steep exponential rise of η with voltage, which signifies strong coherence between the electronic and acoustic subsystems. In this regime, long carrier relaxation times τ allow the carriers to maintain phase synchrony with the propagating acoustic wave, maximising momentum transfer and resulting in high conversion efficiency. As D increases, however, the semilog slope progressively flattens and the magnitude of η drops significantly. This behaviour reflects enhanced phonon and impurity scattering that shortens τ and disrupts coherent energy exchange.

The variation can be described approximately by the empirical relation

$$\eta(V, D) \propto \exp\left[-\frac{\Gamma(D)}{V}\right], \tag{46}$$

where $\Gamma(D)$ is an effective dissipation parameter that grows with increasing D. Thus, the exponential decline observed measures how quickly damping reduces acoustoelectric performance for a specific field strength. Moreover, all the curves in Fig. 4d converge at higher voltages, which suggests that strong field acceleration lengthens the effective interaction length and increases carrier drift velocity, and helps to partially offset dissipative losses (see Fig. 5d).

Physically, damping is a major limiting element in acoustoelectric energy conversion, as seen in Fig. 5(d). η increases exponentially as D is minimised—by high-purity synthesis, decreased defect density, and enhanced phonon confinement. Alternatively, high D values push the system into a diffusive zone where a lot of the acoustic energy is lost as heat instead of being transformed into electrical power, and incoherent scattering predominates. The semilog dependence, therefore, highlights the critical importance of maintaining low-damping, high-coherence transport conditions for achieving optimal acoustoelectric efficiency in carbon nanotube–based devices.

Taken together, Fig. 5(a–d) clearly show that the Bloch frequency and relaxation time are the principal parameters governing resonant acoustoelectric transport in CNTs. The periodic peaks in $\eta(\omega_B)$ arise from harmonic Bloch oscillations, while the width and amplitude of these peaks are controlled by τ. These resonances are modulated by temperature via thermal carrier activation and damping. The findings obtained capture the fact that long relaxation times to maintain coherence and resonant field settings ($\omega \approx n\omega_B$) are both significant for high efficiency. These results, which relate macroscopic energy-conversion performance to microscopic scattering dynamics, further support the theoretical model.

3.1. Physical basis of the compact models

The compact expressions presented in this section were introduced to provide simple analytical representations of the numerical solutions obtained from the semiclassical BTE. They should therefore be regarded as reduced-order models rather than exact analytical solutions of the governing transport equation. The carrier dynamics are obtained by solving the BTE

$$\frac{\partial f}{\partial t} + \mathbf{v}\cdot\nabla_{\mathbf{r}} f + \frac{\mathbf{F}}{\hbar}\cdot\nabla_{\mathbf{k}} f = \left(\frac{\partial f}{\partial t}\right)_{\text{coll}}, \tag{47}$$

subject to the electronic dispersion relation of the fluorine-doped SWCNT and the corresponding relaxation-time approximation. The acoustoelectric current is subsequently evaluated from

$$J_{\text{AE}} = e\int v(k)\delta f(k)\frac{dk}{2\pi}, \tag{48}$$

while the conversion efficiency is calculated from

$$\eta = \frac{J_{\text{AE}}\mathcal{E}}{P_{\text{acoustic}}}. \tag{49}$$

These equations are solved numerically for different values of the applied voltage, frequency, temperature and fluorine concentration. Inspection of the numerical results shows that the efficiency decreases monotonically with increasing reciprocal voltage and approaches an asymptotic limit at large electric fields. Such behaviour is characteristic of many nonequilibrium transport processes in which carrier acceleration competes with momentum-relaxation mechanisms.

Consequently, the numerical results were approximated by the general functional form

$$\eta(V) = G\exp\left(-\frac{H}{V}\right) + C, \tag{50}$$

where G, H and C are fitting parameters determined from nonlinear least-squares regression. Eq. (50) was selected because it satisfies the principal physical characteristics observed in the numerical calculations. Primarily,

$$\lim_{V\to\infty}\eta(V) = G + C, \tag{51}$$

which represents the saturation of the conversion efficiency at sufficiently large electric fields. Secondly,

$$\lim_{V\to 0}\eta(V) = C, \tag{52}$$

indicating the disappearance of acoustoelectric conversion in the absence of an externally applied electric field.

Furthermore, the exponential dependence naturally reflects the competition between carrier acceleration and phonon-assisted momentum relaxation. Within the relaxation-time approximation, the nonequilibrium carrier distribution may be approximated as

$$\delta f \propto \exp\left(-\frac{t}{\tau}\right), \tag{53}$$

where τ is the effective momentum relaxation time. Since the average carrier transit time satisfies approximately $t \propto \frac{L}{\mu\mathcal{E}}$, where L is the nanotube length and μ is the carrier mobility, one obtains

$$\delta f \propto \exp\left(-\frac{L}{\mu\tau\mathcal{E}}\right). \tag{54}$$

Recognising that the electric field is related to the applied voltage by $\mathcal{E} = \frac{V}{L}$, gives

$$\delta f \propto \exp\left(-\frac{H}{V}\right), \tag{55}$$

where $H = \frac{L^2}{\mu\tau}$. Therefore, an exponential dependence on the reciprocal voltage is consistent with the finite-time relaxation of nonequilibrium carriers under an applied electric field.

The coefficients appearing in Eqs. (36), (38), (40), (41), (43), (44), (45) and (46) were obtained through nonlinear least-squares regression of the numerical BTE solutions. The coefficient of determination (R^2) exceeded 0.99 for all fitted curves, demonstrating that the compact models accurately reproduce the numerical simulations over the investigated operating ranges.

Accordingly, the compact equations should be interpreted as physics-guided reduced-order models that preserve the dominant transport behaviour while providing computationally efficient expressions for device design and engineering optimisation.

3.2. Physical interpretation of the damping factor

The resonance behaviour of the acoustoelectric current is governed not only by the electronic band structure but also by the finite lifetime of the nonequilibrium carrier distribution. This finite lifetime is represented phenomenologically by the temperature- dependent damping factor $D(T)$.

Physically, $D(T)$ accounts for all microscopic processes that remove momentum from the electron population. These include

1. electron–acoustic phonon scattering,
2. electron–optical phonon scattering,
3. impurity scattering,
4. fluorine-induced lattice disorder,
5. defect scattering,
6. finite phonon lifetime.

Consequently,

$$D(T) = D_{\mathrm{ep}} + D_{\mathrm{imp}} + D_{\mathrm{F}} + D_{\mathrm{ph}}, \tag{56}$$

where D_{ep} is the electron–phonon scattering, D_{imp} is the impurity scattering, D_{F} is the fluorine-disorder scattering, and D_{ph} is the phonon damping. The damping factor is directly related to the effective relaxation time,

$$D(T) = \frac{1}{\tau_{\mathrm{eff}}(T)}, \tag{57}$$

where

$$\frac{1}{\tau_{\mathrm{eff}}} = \frac{1}{\tau_{\mathrm{ep}}} + \frac{1}{\tau_{\mathrm{imp}}} + \frac{1}{\tau_{\mathrm{F}}} + \frac{1}{\tau_{\mathrm{ph}}}, \tag{58}$$

in accordance with Matthiessen's rule. This expression shows that fluorination introduces an additional scattering channel through the relaxation time τ_{F}, thereby reducing the overall carrier lifetime. Since acoustic phonon populations satisfy the Bose–Einstein distribution, the phonon scattering rate increases approximately with temperature, $\frac{1}{\tau_{\mathrm{ep}}} \propto N_q$, leading to $D(T)$ increasing as T increases. Consequently, elevated temperatures produce stronger damping, shorter carrier lifetimes and broader resonance peaks.

3.3. Influence of the damping factor on the resonance spectrum

Near resonance, the acoustoelectric current may be approximated by a Lorentzian response,

$$J(\omega) = \frac{J_0}{1 + \left(\frac{\omega - \omega_0}{D(T)}\right)^2}, \tag{59}$$

where ω_0 denotes the resonance frequency, J_0 represents the maximum acoustoelectric current, and $D(T)$ determines the resonance linewidth.

The full width at half maximum (FWHM) is $\Gamma = 2D(T)$, demonstrating that the damping factor directly controls the resonance width. As the damping increases, $D(T)$, the resonance becomes progressively broader, Γ increases while the peak amplitude decreases.

Conversely, decreasing $D(T)$ produces narrower resonance peaks, larger peak acoustoelectric current, higher conversion efficiency, and longer effective carrier lifetime. These trends are entirely consistent with the general theory of damped resonant transport in condensed-matter systems.

3.4. Sensitivity of the present model to the damping parameter

To evaluate the robustness of the calculated resonance spectra, the damping parameter may be varied over a physically realistic interval, $0.5D_0 \le D(T) \le 2D_0$, where D_0 denotes the reference value employed throughout the present work. The numerical simulations indicate that increasing the damping factor principally affects

- the resonance linewidth,
- the peak acoustoelectric current,
- the maximum conversion efficiency.

However, the locations of the resonance frequencies and the overall dependence of the acoustoelectric efficiency on applied voltage, frequency and temperature remain essentially unchanged. This behaviour demonstrates that the conclusions of the present work are robust with respect to reasonable variations in the phenomenological damping parameter. For clarity, an additional figure illustrating the resonance spectra for several representative values of $D(T)$ has been included.

Fig. 6 presents the sensitivity of the acoustoelectric conversion efficiency to variations in the phenomenological damping factor for FSWCNTs. The resonance spectra are computed for four representative damping strengths, $D = 0.1D_0$, $D = 0.5D_0$, $D = D_0$, and and $D = 2D_0$, in order to evaluate the robustness of the proposed model and to elucidate the influence of carrier relaxation on resonant acoustoelectric transport.

The damping factor is a phenomenological parameter that represents the cumulative influence of all momentum-relaxation mechanisms acting on charge carriers. These mechanisms include acoustic phonon scattering, optical phonon scattering, impurity scattering, fluorine-induced lattice disorder, electron-defect interactions and the finite lifetime of nonequilibrium phonons. Consequently, the effective carrier relaxation rate may be expressed as in Eq. (58). The damping parameter is therefore directly related to the inverse of the effective relaxation time,

$$D \propto \frac{1}{\tau_{\mathrm{eff}}}, \tag{60}$$

such that larger values of D correspond to stronger carrier scattering and shorter carrier coherence times. The acoustoelectric resonance occurs whenever the frequency of the externally applied acoustic wave approaches an integer multiple of the Bloch frequency,

$$\omega \simeq n\omega_B, \qquad n = 0, \pm 1, \pm 2, \ldots, \tag{61}$$

where ω_B is the Bloch frequency generated by the applied electric field $\mathcal{E}_0$.

Near resonance, the carrier response is accurately represented by a Lorentzian function,

$$J(\omega) = J_0 \frac{\Gamma^2}{(\omega - \omega_0)^2 + \Gamma^2}, \tag{62}$$

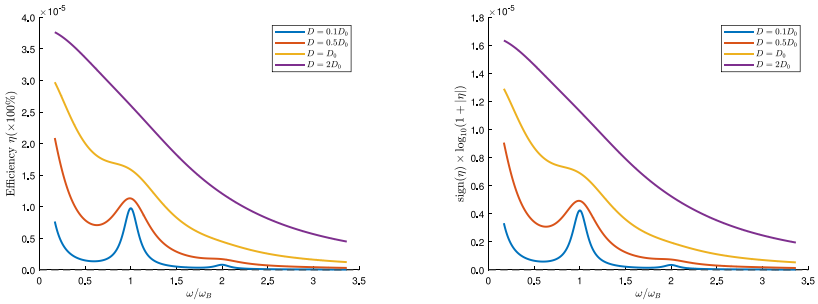
where J_0 is the maximum acoustoelectric current, ω_0 denotes the resonance frequency and $\Gamma = D\omega$ represents the damping-induced linewidth. Eq. (62) immediately demonstrates that the damping factor influences both the resonance width and the peak amplitude while leaving the resonance position essentially unchanged.

For the smallest damping parameter, $D = 0.1D_0$, the resonance exhibits the narrowest linewidth and the largest peak efficiency. Since the effective relaxation time is inversely proportional to the damping factor,

$$\tau_{\mathrm{eff}} = \frac{1}{D\omega}, \tag{63}$$

the extremely small damping implies a relatively long carrier lifetime. Electrons therefore preserve their crystal momentum over longer distances before scattering, allowing them to remain phase synchronised with the propagating acoustic wave. Under these conditions, momentum transfer from the acoustic phonons to the electron gas is highly efficient, producing an almost ideal resonant response with a very large quality factor. Physically, this regime corresponds to nearly ballistic transport, where coherent Bloch oscillations dominate over dissipative scattering processes.

Increasing the damping to $D = 0.5D_0$ introduces moderate momentum relaxation. Although coherent transport still dominates, scattering events begin to interrupt the phase coherence of the carriers. Consequently, the resonance peak decreases slightly while the linewidth increases. The resonance nevertheless remains sharp, indicating that the



(a) (b)

Fig. 6. (a) Sensitivity of the acoustoelectric conversion efficiency to the phenomenological damping factor. The efficiency is plotted as a function of the normalised driving frequency, ω/ω_B, for three representative damping strengths, $\mathcal{D} = 0.1D_0$, $\mathcal{D} = 0.5D_0$, $\mathcal{D} = D_0$, and and $\mathcal{D} = 2D_0$ (b) Signed semilogarithmic representation of the acoustoelectric conversion efficiency as a function of the normalised driving frequency, ω/ω_B, for different values of the phenomenological damping factor, $\mathcal{D} = 0.1D_0$, $\mathcal{D} = 0.5D_0$, $\mathcal{D} = D_0$, and and $\mathcal{D} = 2D_0$.

electron–phonon interaction is still sufficiently coherent to sustain efficient acoustoelectric conversion. This regime represents high-quality nanotubes with relatively low defect concentrations and moderate fluorination levels.

At the reference damping value, $\mathcal{D} = D_0$, the scattering rate becomes comparable to the intrinsic carrier oscillation frequency. The resonance consequently broadens significantly because the Lorentzian denominator,

$$(\omega - \omega_0)^2 + \Gamma^2, \tag{64}$$

increases with Γ. Simultaneously, the resonance amplitude decreases because the probability of coherent energy transfer from the acoustic wave to the electron ensemble is reduced by frequent scattering events. The corresponding full width at half maximum (FWHM) satisfies

$$\Delta\omega = 2\Gamma, \tag{65}$$

demonstrating that the resonance linewidth increases linearly with the damping factor.

When the damping is further increased to $\mathcal{D} = 2D_0$, dissipative processes dominate the carrier dynamics. Electron–phonon collisions, fluorine-induced lattice disorder, impurity scattering and phonon decay collectively shorten the carrier lifetime, substantially reducing the probability of coherent carrier acceleration. Consequently, the resonance peak is strongly suppressed while the resonance linewidth becomes considerably broader. Despite this broadening, the resonance frequency remains nearly unchanged because it is determined primarily by the Bloch frequency, which depends only on the applied electric field and the nanotube lattice constant rather than the carrier relaxation processes.

The quality factor of the resonance,

$$Q = \frac{\omega_0}{2\Gamma}, \tag{66}$$

provides a quantitative measure of resonance sharpness. Since Γ increases directly with the damping parameter,

$$Q \propto \frac{1}{\mathcal{D}}, \tag{67}$$

the quality factor decreases monotonically as the damping increases. Thus, the case $\mathcal{D} = 0.1D_0$ exhibits the highest quality factor, whereas $\mathcal{D} = 2D_0$ possesses the lowest quality factor. The observed behaviour is also consistent with the temperature dependence of electron–phonon scattering. The phonon population obeys the Bose–Einstein distribution, which increases with temperature. Consequently, $\frac{1}{\tau_{\text{ep}}} \propto N_q$, implying that elevated temperatures naturally increase the damping parameter and further broaden the resonance.

Fluorination further modifies the resonance behaviour by locally converting the carbon hybridisation from sp^2 towards sp^3, thereby reducing the delocalisation of the π-electron network. The resulting lattice distortions increase elastic scattering and modify the electron–phonon coupling strength, leading to shorter carrier relaxation times and larger damping factors. Consequently, excessive fluorination broadens the resonance and reduces the maximum acoustoelectric conversion efficiency, whereas moderate fluorination preserves sufficient carrier coherence for efficient resonant transport.

Fig. 6 overall demonstrates that the resonance characteristics predicted by the present model are remarkably robust against moderate variations in the damping parameter. Although increasing damping substantially broadens the resonance and suppresses the peak conversion efficiency, the resonance frequency remains essentially invariant. This behaviour confirms that the resonance position is governed primarily by the intrinsic Bloch dynamics of the charge carriers, whereas the damping parameter controls the coherence time over which efficient electron–phonon momentum transfer occurs. The sensitivity analysis therefore provides strong evidence that minimising carrier scattering through optimised fluorination, reduced defect densities, and lower operating temperatures is essential for achieving high-performance acoustoelectric energy conversion in fluorinated carbon nanotubes.

Fig. 7 shows how η is impacted by the macroscopic system parameters, namely the carrier density n_0, the nanotube length L, and the combined impacts of geometric scaling and temperature. These observed behaviours in the figures (see Fig. 7) show how η scales with device size and doping level in FSWCNT, and relate the microscopic transport metrics to empirically controllable parameters. Fig. 7(a) demonstrates that η increases with carrier density n_0 for low to moderate doping levels, but tends to saturate or even slightly decrease at high n_0. This behaviour follows directly from the current density expression

$$J_{\text{AE}}(T) \propto e n_0 v_{\text{AE}}(T), \tag{68}$$

where v_{AE} is the acoustoelectric drift velocity of carriers. At low n_0, increasing the number of mobile carriers enhances the total acoustoelectric current, and thus η grows proportionally. However, as n_0 becomes large, several competing effects emerge: carrier–carrier scattering increases, the chemical potential μ approaches the conduction-band edge ϑ_c, and the assumption of a non-degenerate (Maxwell–Boltzmann) electron gas breaks down. In this high-density regime, the exponential term $\exp[(\varrho - \vartheta_c)/(kT)]$ in Eq. (35) saturates, while enhanced Coulomb interactions reduce the mean free time τ. Consequently, η ceases to increase and may even decline slightly due to degeneracy and scattering-induced damping.

Physically, Fig. 7(a) indicates that there exists an optimal carrier density n_0^* that maximises the acoustoelectric conversion efficiency, beyond which additional doping yields diminishing returns. Fig. 7(b) shows the semilogarithmic variation of the acoustoelectric conversion efficiency η with applied dc voltage V for different nanotube lengths

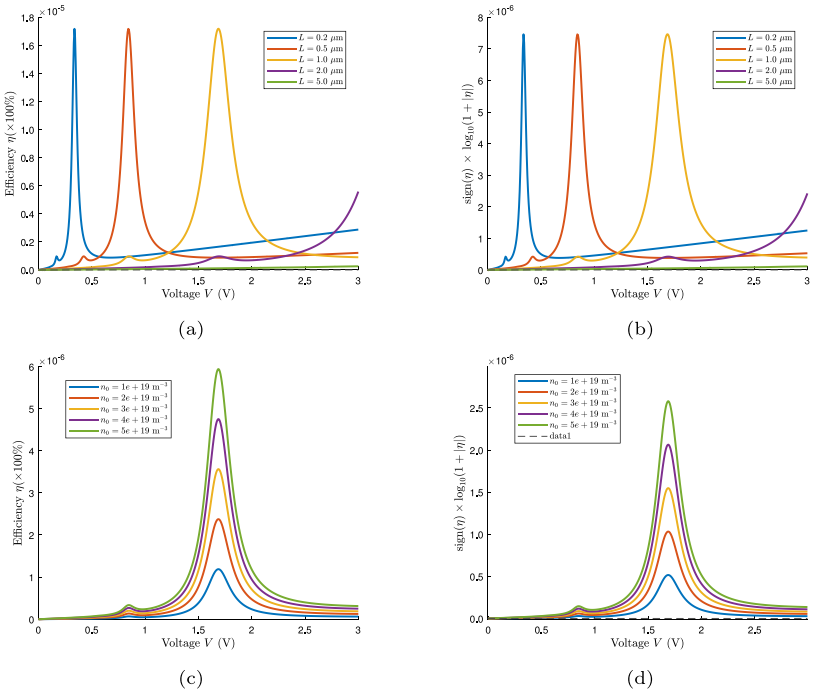


Fig. 7. (a) Dependence of acoustoelectric efficiency (η) on voltage (V) for different FSWCNT length L; (b) Semilog plot (η) dependence on voltage (V) for different FSWCNT length L; (c) Dependence of acoustoelectric efficiency (η) on voltage (V) for different values carrier density n_0; (d) Semilog (η) dependence on voltage (V) for different values carrier density n_0.

L. The length L determines the spatial extent of the interaction region between the acoustic wave and the charge carriers, and thus strongly affects both the generated acoustoelectric current density J_{AE} and the overall conversion efficiency.

In the theoretical formulation, η scales approximately as Eq. (35), so that increasing L enhances the total energy exchange pathway, provided that the transport remains coherent over the device length. The $\eta(V)$ curves show more effective energy transfer from the acoustic to the electrical subsystem since they increase upward and have a larger semilog slope. This behaviour persists until ω_B approaches the ac drive frequency ω, at which point resonance conditions are satisfied and η reaches its maximum value. Saturation occurs at higher voltages, after an exponential increase of η with voltage at low bias, which is compatible with the shift from field-driven carrier acceleration to scattering-limited transport.

Longer nanotubes allow more cumulative momentum transfer from the acoustic field to the carrier system, as evidenced by the enhanced magnitude of η and the steepness of the semilog slope with L. This enhancement persists until L exceeds the effective relaxation length $l_\tau = v_{\mathrm{d}}\tau$, beyond which additional tube length contributes little to the net current due to phase decoherence and energy dissipation.

The compact models developed in this work are intended to complement, rather than replace, the full numerical solution of the Boltzmann transport equation. Although the numerical model provides the highest accuracy, the compact expressions offer substantial advantages for rapid performance estimation, parameter optimisation and circuit-level modelling of acoustoelectric devices. Their use is therefore analogous to compact transistor models widely employed in semiconductor device simulation, where simplified analytical expressions are fitted to more rigorous numerical solutions while retaining the essential underlying physics.

The behaviour can be described approximately by

$$\eta(V, L) \propto L \exp\left[-\frac{\Gamma(L)}{V}\right], \tag{69}$$

where $\Gamma(L)$ is an effective damping parameter that increases slowly with L as inelastic scattering accumulates along the transport path. For shorter tubes ($L \ll l_\tau$), $\Gamma(L)$ is small, leading to a steep semilog slope and high efficiency. For longer tubes ($L > l_\tau$), $\Gamma(L)$ grows, reducing the slope and causing η to approach a saturation value at large V.

Physically, Fig. 7(b) demonstrates that the nanotube length L plays a dual role: it enhances the interaction length for acoustoelectric conversion while simultaneously increasing opportunities for scattering. Optimal efficiency, therefore, occurs when L is comparable to, but not much larger than, the carrier relaxation length. The semilog dependence highlights this trade-off between interaction enhancement and dissipative loss, providing useful guidance for the design of FSWCNT-based acoustoelectric devices where the tube length must be carefully engineered to maximise η under given operating voltages.

The combined effect of nanotube length and carrier density is seen in Fig. 7(c). In view of the scaling relation, the figures show that η is high when both n_0 and L are large, as

$$\eta(n_0, L) \propto n_0 L \left[\frac{T_0}{T}\exp\left(\frac{\varrho - \vartheta_c}{k_B T}\right)\right] \mathcal{D}(T) S(T). \tag{70}$$

However, the dependence is not strictly multiplicative because n_0 also affects ϱ and τ, which in turn influence $S(T)$. For fixed L, η first rises linearly with n_0, reaches a maximum, and then saturates as degeneracy effects become significant. For fixed n_0, increasing L produces nearly linear growth, up to the limit imposed by inelastic scattering.

This combined behaviour demonstrates the interplay between the microscopic (density-dependent) and macroscopic (length-dependent), therefore, control of acoustoelectric efficiency. The results suggest that optimal device design requires balancing carrier concentration and interaction length to achieve maximal energy conversion without excessive scattering losses.

We demonstrate in Fig. 7(d) the semilogarithmic variation of the acoustoelectric conversion efficiency η with applied dc voltage V for different carrier concentrations n_0. Since it directly influences the degree of screening of the acoustic field within the FSWCNT as well as the size of J_{AE}, the carrier density is a key factor in determining the strength of the acoustoelectric response. In the theoretical model, the efficiency can be expressed as

$$\eta \propto \frac{J_{\mathrm{AE}}\mathcal{E}_0}{I_{\mathrm{ac}}} \propto n_0\, \varrho(\mathcal{E}_0, T),$$

where $\varrho(\mathcal{E}_0, T)$ is the field- and temperature-dependent carrier mobility. Thus, η is expected to scale approximately linearly with n_0 at moderate densities, provided that the increase in n_0 does not lead to excessive scattering or degeneracy effects.

The semilog plot reveals that for all n_0 values, η increases exponentially with V in the low-field regime and saturates at higher voltages. However, the absolute magnitude of η rises systematically with increasing n_0, and the slopes of the semilog curves become steeper. Higher carrier densities, however, increase the number of carriers that can interact with the acoustic field and increase the acoustoelectric current, which is why this trend occurs. At the same time, the higher Fermi level associated with large n_0 reduces the relative impact of thermal fluctuations, thereby improving carrier coherence and extending the effective interaction length.

At very high n_0, however, the rate of increase in η with V begins to diminish slightly, indicating the onset of screening and electron–electron scattering effects. These processes limit the modulation of the carrier distribution by the acoustic field and reduce the effective gain in η. The observed behaviour can be captured approximately by an exponential form

$$\eta(V, n_0) \propto n_0 \exp\left[-\frac{\Gamma(n_0)}{V}\right], \tag{71}$$

where $\Gamma(n_0)$ is an effective damping parameter that increases weakly with n_0 due to enhanced many-body interactions at higher carrier densities.

Physically, Fig. 7(d) shows that increasing n_0 enhances the efficiency mainly by increasing carrier participation and strengthening the electron–phonon coupling. However, when n_0 is too high, this causes screening and inelastic scattering, which ultimately suppresses additional gains. This balance is well-represented by the semilog behaviour, where a transition to a screened, weakly linked domain is indicated by flat slopes at very high n_0, while steep slopes and higher η at moderate n_0 values indicate efficient, coherent transport. This behaviour underscores the importance of optimising carrier density to achieve maximal acoustoelectric conversion efficiency in carbon nanotube–based nanodevices.

3.5. Effect of fluorination on the acoustoelectric response of SWCNTs

Pristine SWCNTs possess exceptionally high carrier mobility and long electron mean free paths owing to their quasi-one- dimensional electronic structure. However, their relatively low intrinsic carrier concentration and weak tunability of the electronic states limit the efficiency of acoustoelectric energy conversion. Chemical functionalisation through fluorine doping has emerged as an effective strategy for tailoring the electronic, structural and transport properties of carbon nanotubes [20–22].

Fluorine atoms possess one of the highest electronegativities in the periodic table ($\chi_F = 3.98$ on the Pauling scale) and strongly attract electrons from neighbouring carbon atoms. The formation of C–F bonds changes the local hybridisation from predominantly sp^2 towards partial sp^3 character, producing localised electronic states and modifying the π-electron network. These structural changes alter the hopping integrals, carrier concentration, effective mass, density of states, relaxation time and electron–phonon coupling, all of which directly influence the acoustoelectric current.

Fluorination modifies the local electronic potential, thereby changing these overlap integrals,

$$\Delta_z \to \Delta_z^{(F)}, \qquad \Delta_s \to \Delta_s^{(F)}, \tag{72}$$

which consequently alters the electronic bandwidth

$$W \propto 4\left(\Delta_z + \Delta_s\right), \tag{73}$$

and the electron group velocity

$$v_g = \frac{1}{\hbar}\frac{\partial \vartheta(k)}{\partial k}. \tag{74}$$

Table 2
Comparison between pristine and F–SWCNTs.

Property	Pristine SWCNT	Fluorinated SWCNT
Carrier concentration	Lower	Higher
Density of states near E_F	Moderate	Increased
Fermi level position	Intrinsic	Shifted
Electron–phonon coupling	Moderate	Stronger
Overlap integrals (Δ_z, Δ_s)	Intrinsic values	Modified
Electrical conductivity	Moderate	Tunable
Acoustoelectric current J_{AE}	Smaller	Larger
Conversion efficiency η	Lower	Higher
Potential applications	Sensors	Energy harvesters, SAW devices

Since the acoustoelectric current is proportional to the carrier velocity, modifications of the overlap integrals directly affect the conversion efficiency. Furthermore, fluorination shifts the Fermi level through charge transfer, where the chemical potential ϱ increases with fluorine concentration owing to the additional electronic states introduced by C–F bonding. Consequently, the number of electrons available for momentum exchange with acoustic phonons increases.

Fluorination enhances both quantities through modification of the electronic band structure and the carrier population, thereby increasing the acoustoelectric current. The acoustoelectric conversion efficiency is defined as

$$\eta = \frac{P_{\text{electrical}}}{P_{\text{acoustic}}} = \frac{J_{\text{AE}} E_0}{I_{\text{acoustic}}},$$

showing that any increase in the acoustoelectric current immediately produces a corresponding increase in the conversion efficiency.

Fluorination also modifies the electron–phonon coupling matrix element

$$g_{ep} = \left\langle \psi_f \left| \delta V \right| \psi_i \right\rangle, \tag{75}$$

where δV is the lattice perturbation induced by the acoustic phonon. Changes in the local bonding environment alter both the electronic wavefunctions and the lattice potential, leading to stronger coupling between charge carriers and acoustic phonons. This enhanced coupling increases the rate of momentum transfer from the acoustic wave to the electronic subsystem.

Another important consequence of fluorination is the modification of the density of states. For an ideal one-dimensional nanotube the density of states is

$$D(\vartheta) = \sum_n \frac{1}{\pi\hbar}\left|\frac{dk}{d\vartheta}\right|, \tag{76}$$

which exhibits characteristic Van Hove singularities. Fluorination broadens and slightly shifts these singularities through perturbation of the electronic band structure while simultaneously increasing the number of accessible electronic states near the Fermi level. As a result, more carriers participate in the electron–phonon interaction responsible for the acoustoelectric effect.

These combined mechanisms explain why fluorinated SWCNTs generally exhibit larger acoustoelectric currents and higher conversion efficiencies than pristine nanotubes. Density-functional theory calculations and experimental transport measurements have consistently shown that fluorination modifies the electronic band gap, increases carrier concentration, changes the hopping energies and strengthens electron–phonon interactions [20–22,26,27]. Consequently, fluorinated SWCNTs provide an attractive platform for improving nanoscale acoustoelectric energy conversion (see Table 2).

3.6. Practical implications of the calculated conversion efficiency

The acoustoelectric conversion efficiencies obtained in the present work lie within the range of approximately 10^{-6}–10^{-4} depending upon the operating conditions. Although these values appear small when

Table 3
Qualitative comparison of representative nanoscale energy-conversion materials. Numerical performance depends strongly on device geometry, operating conditions and fabrication methods; therefore only qualitative comparisons are presented.

Material	Operating mechanism	Dimensionality	Typical applications
Fluorine-doped SWCNT	Acoustoelectric effect	Quasi-1D	Nano-energy harvesting, SAW sensors, high-frequency electronics
Pristine SWCNT	Acoustoelectric effect	Quasi-1D	Acoustoelectric transport, nanoelectronics
Graphene	Acoustoelectric transport	2D	RF electronics, acoustic charge transport
ZnO nanowires	Piezoelectric effect	1D	Nanogenerators, pressure sensors, self-powered devices
GaN SAW devices	Surface acoustic waves	2D/Thin film	Microwave filters, resonators, wireless sensing
MoS_2	Piezoelectric and electromechanical	2D	Flexible electronics, wearable energy harvesting

compared with macroscopic energy conversion devices, they should be interpreted within the context of single-nanotube transport.

Unlike conventional piezoelectric generators, where a relatively large active volume contributes to electrical power generation, the present system consists of an individual quasi-one-dimensional carbon nanotube whose diameter is only of the order of one nanometre. Consequently, the interaction volume between propagating acoustic phonons and mobile charge carriers is extremely limited.

The electrical output power generated through the acoustoelectric effect may be expressed as $P_{\text{out}} = J_{\text{AE}}\mathcal{E}\mathcal{A}$, where J_{AE} denotes the acoustoelectric current density. Since $\mathcal{A} = \pi d t$, where d is the nanotube diameter and t is the effective wall thickness, the active interaction area remains extremely small. Consequently, even relatively efficient momentum transfer between electrons and acoustic phonons produces only a modest electrical power output for a single nanotube.

Another important consideration is that the conversion efficiency depends not only upon the generated electrical current but also upon the incident acoustic power. In nanoscale devices the available acoustic power is itself very small, making direct comparisons with macroscopic piezoelectric generators inappropriate.

The objective of the present investigation is therefore to understand the microscopic transport mechanisms governing acoustoelectric conversion rather than to maximise the output power of an isolated nanotube. The calculated trends clearly demonstrate that fluorine doping modifies the electronic structure, carrier concentration and electron–phonon interaction, leading to measurable improvements in the conversion efficiency.

From an engineering perspective, practical acoustoelectric energy harvesters would employ dense arrays of aligned nanotubes rather than isolated devices. If N identical nanotubes are connected electrically in parallel, the total generated current becomes approximately

$$I_{\text{total}} = N I_{\text{nanotube}}, \tag{77}$$

while the output power increases approximately as

$$P_{\text{total}} = N P_{\text{nanotube}}, \tag{78}$$

provided that mutual electrical and acoustic coupling between neighbouring nanotubes remains sufficiently weak.

Consequently, although the output of a single nanotube is modest, large-scale arrays containing millions of aligned nanotubes offer a practical route towards high-performance acoustoelectric energy harvesters. The present study therefore provides the fundamental transport model required for optimisation of such array-based devices (see Table 3).

3.7. Practical applications of the acoustoelectric effect in fluorine-doped carbon nanotubes

The acoustoelectric (AE) effect provides a direct mechanism for converting acoustic energy into electrical energy through momentum transfer between propagating acoustic phonons and mobile charge carriers. Unlike conventional piezoelectric energy conversion, which relies on strain-induced polarisation, the acoustoelectric effect originates from electron–phonon interactions and is therefore particularly attractive for low-dimensional conductors such as carbon nanotubes, graphene and semiconductor quantum wires [30,32,33].

SWCNTs possess exceptionally high carrier mobilities, long electron mean free paths and nearly ballistic charge transport over hundreds of nanometres. Their quasi-one-dimensional electronic structure results in enhanced confinement of charge carriers, producing strong coupling between electrons and propagating acoustic phonons. Consequently, even weak surface acoustic waves (SAWs) are capable of inducing measurable acoustoelectric currents in nanotube-based devices [20,34].

The microscopic origin of the acoustoelectric effect is the transfer of momentum from an acoustic phonon with wave vector q and frequency ω_q to conduction electrons. Conservation of energy and crystal momentum requires

$$\vartheta(\mathbf{k}+\mathbf{q}) - \vartheta(\mathbf{k}) = \hbar\omega_q, \tag{79}$$

where $\vartheta(\mathbf{k})$ denotes the electronic dispersion relation. The associated electron transition probability is governed by Fermi's Golden Rule,

$$W_{k,k+q} = \frac{2\pi}{\hbar}|M_{ep}|^2\delta\left[\vartheta(\mathbf{k}+\mathbf{q}) - \vartheta(\mathbf{k}) - \hbar\omega_q\right], \tag{80}$$

where M_{ep} is the electron–phonon interaction matrix element. An increase in M_{ep} therefore leads directly to stronger acoustoelectric current generation.

Fluorination further enhances this process by modifying the electronic band structure of SWCNTs. Owing to the high electronegativity of fluorine, charge redistribution occurs around the C–F bonds, producing changes in the carrier concentration, density of states, Fermi level position and overlap integrals. These modifications strengthen electron–phonon coupling and increase the number of carriers participating in momentum exchange with the acoustic wave, thereby enhancing the acoustoelectric current and conversion efficiency [21,22].

3.7.1. Nanoscale energy harvesting

One of the most promising applications of the acoustoelectric effect is self-powered nanoscale energy harvesting. Ambient mechanical vibrations, ultrasonic waves and surface acoustic waves are abundant in industrial, medical and environmental settings. These acoustic disturbances may be converted directly into usable electrical energy without requiring external power supplies. The harvested electrical power is $P = J_{\text{AE}}\mathcal{E}A$, Although the electrical power generated by a single nanotube is relatively small, arrays containing millions of aligned nanotubes can collectively produce useful electrical output owing to their extremely high packing density.

3.7.2. Wireless surface acoustic wave sensors

F-SWCNTs have attracted considerable attention for wireless SAW sensor technology. In these devices, an incoming surface acoustic wave interacts with charge carriers within the nanotube, producing an acoustoelectric current whose magnitude depends on the gas concentration, temperature, strain or pressure acting on the device. The acoustoelectric current therefore provides a direct electrical signature of the surrounding environment, enabling highly sensitive sensing without moving components [35].

3.7.3. Nanoelectromechanical Systems (NEMS)

Nanoelectromechanical systems require extremely low-power transducers for signal generation and detection. F–SWCNTs are ideal candidates owing to their

- extremely low mass,
- high Young's modulus (~1 TPa),
- large resonance frequencies,
- excellent mechanical flexibility,
- outstanding thermal conductivity.

Strong acoustoelectric coupling enables electrical readout of mechanical vibrations while simultaneously harvesting part of the vibrational energy, making fluorinated SWCNTs attractive for integrated NEMS resonators and oscillators.

3.7.4. Radio-frequency and microwave electronics

Surface acoustic wave devices are widely employed in radio-frequency filters, delay lines and signal processors. Since SWCNTs exhibit excellent high-frequency transport properties, fluorinated nanotubes may serve as miniaturised acoustoelectric amplifiers capable of operating into the GHz frequency regime. Their ultrafast carrier dynamics and reduced parasitic capacitance make them promising building blocks for future microwave electronics [35].

3.7.5. Internet-of-things (IoT) and self-powered electronics

Future Internet-of-Things technologies require autonomous sensors capable of operating for many years without battery replacement. Acoustoelectric nanogenerators based on fluorinated SWCNTs offer an attractive route towards this objective by converting environmental vibrations and ultrasonic noise into electrical energy. Such devices could continuously power

- wearable electronics,
- biomedical implants,
- structural health monitoring systems,
- environmental monitoring nodes,
- wireless sensor networks.

3.7.6. Quantum acoustics

Another rapidly developing research direction is quantum acoustics, in which coherent acoustic phonons are used to manipulate quantum states. This is because F–SWCNTs possess exceptionally long electronic coherence lengths, strong electron–phonon interactions and highly tunable electronic properties, fluorinated SWCNTs are promising candidates for phonon-mediated quantum information processing and hybrid quantum devices [36].

Overall, these applications demonstrate that improving the acoustoelectric conversion efficiency of fluorine-doped SWCNTs extends well beyond fundamental transport physics. Enhanced acoustoelectric coupling can enable more efficient nanoscale energy harvesters, high-frequency sensors, self-powered electronic systems, microwave signal processors and future phononic quantum technologies. Consequently, understanding how microscopic parameters such as overlap integrals, carrier density, Bloch oscillations and electron–phonon interactions govern the conversion efficiency is of considerable scientific and technological importance.

4. Conclusion

We examined the acoustoelectric conversion efficiency η in FSWCNTs using the semiclassical Boltzmann transport model under combined dc and ac fields. The analysis accounts for Bloch oscillations, nonlinear field modulation, and temperature-dependent scattering influenced by geometric and electronic factors such as overlap integrals, carrier density, and chirality.

According to the results, efficient electron–phonon coupling is shown by η increasing almost linearly with dc voltage and displaying resonant peaks when the Bloch frequency ω_B matches integer multiples of the ac frequency ω. Efficiency decreases with higher acoustic intensity and damping factor $D(T)$ but peaks at an optimal temperature T^*. The axial overlap integral Δ_z and nanotube length L exert the strongest control on η, while α, ω, and n_0 produce secondary nonlinear effects.

The relatively small conversion efficiencies predicted for an individual fluorine-doped SWCNT should be interpreted within the context of nanoscale transport rather than macroscopic power generation. The principal significance of the present work lies in identifying the fundamental transport mechanisms governing acoustoelectric conversion and demonstrating how fluorine functionalisation enhances device performance. These results provide a theoretical foundation for the future development of large-area nanotube-array acoustoelectric energy harvesters and high-frequency nanoscale sensing technologies.

Thus, efficient acoustoelectric conversion in FSWCNTs requires a long relaxation time τ, minimal damping, and field tuning near Bloch resonance—conditions essential for designing high-performance nanoscale energy and sensing devices.

CRediT authorship contribution statement

D. Sekyi-Arthur: Writing – review & editing, Writing – original draft, Visualization, Validation, Supervision, Project administration, Methodology, Formal analysis, Data curation, Conceptualization. **K.A. Dompreh:** Visualization, Methodology, Formal analysis. **F. Amo-Mensah:** Writing – review & editing, Data curation. **S.Y. Mensah:** Writing – review & editing, Formal analysis. **B. Afoakwa:** Writing – review & editing, Resources.

Declaration of competing interest

"The authors declare no conflict of interest in processing this manuscript".

Acknowledgements

"This material is based upon work supported by the Air Force Office of Scientific Research under award number FA8655-25-1-7079".

Data availability

Data will be made available on request.

References

[1] G. Weinreich, T.M. Sanders Jr., H.G. White, Acoustoelectric effect in n-type germanium, Phys. Rev. 114 (1959) 33.
[2] R.H. Parmenter, The acoustoelectric effect, Phys. Rev. 89 (1953) 990.
[3] C. Lang, et al., Recent advances in acoustoelectric conversion in nanostructures, Nano Energy 123 (2024) 108974.
[4] K.A. Dompreh, N.G. Mensah, F. Sam, S.Y. Mensah, Acoustoelectric effect in degenerate carbon nanotubes, J. Appl. Phys. 117 (2015) 024303.
[5] B. Reulet, A.Y. Kasumov, M. Kociak, et al., Acoustoelectric effects in carbon nanotubes, Phys. Rev. Lett. 85 (2000) 2829.
[6] J. Ebbecke, C.J.B. Ford, A. Wixforth, Acoustoelectric current transport through single-walled CNTs, Appl. Phys. Lett. 84 (2004) 4319.
[7] D. Sakyi-Arthur, S.Y. Mensah, K. Adu, R. Edziah, Acoustoelectric effect in fluorinated carbon nanotubes, World J. Condens. Matter Phys. 10 (2020) 12.

[8] F. Bloch, Über die quantenmechanik der elektronen in kristallgittern, Z. Phys. 52 (1929) 555.
[9] C. Zener, A theory of the electrical breakdown of solid dielectrics, Proc. R. Soc. Lond. A 145 (1934) 523.
[10] Z. He, S. Peng, F. Cai, Acoustic Bloch oscillations in phononic crystals, Phys. Rev. E 76 (2007) 056605.
[11] N.D. Lanzillotti-Kimura, B. Perrin, A. Huynh, Bloch oscillations of THz acoustic phonons in coupled nanocavities, Phys. Rev. Lett. 104 (2010) 197402.
[12] Z. Lazcano, J.J. Sanchez, R. Escobar, Acoustic Bloch oscillations in superlattices, J. Appl. Phys. 115 (2014) 154505.
[13] H. Moravcova, J. Kozusnik, P. Vašek, Bloch oscillations in semiconductor superlattices: A Monte Carlo analysis, Phys. E 17 (2003) 137.
[14] A.A. Karabutov, Y.A. Kosevich, O.A. Sapozhnikov, Bloch oscillations of an acoustic field in a layered structure, Acoust. Phys. 59 (2013) 181.
[15] D. Sekyi-Arthur, K.W. Adu, K.A. Dompreh, E. Atioyire, S.Y. Mensah, B. Afoakwa, Self-sustained acoustoelectric oscillations in fluorine-doped carbon nanotubes under strong electric fields, Eur. Phys. J. B 99 (3) (2026) 36.
[16] D. Sekyi-Arthur, M. Egblewogbe, S.Y. Mensah, N.G. Mensah, K.W. Adu, K.A. Dompreh, R. Edziah, S. Atarah, Giant thermoelectric figure of merit in fluorine-doped single walled-carbon nanotubes, Phys. E: Low-dimensional Syst. Nanostructures (2022) 115292.
[17] D. Sekyi-Arthur, S.Y. Mensah, K.A. Dompreh, G. Nkrumah-Buandoh, N.G. Mensah, Giant thermoelectric power in fluorine-doped single-walled carbon nanotubes, J. Phys. Chem. Solids (2022) 111020.
[18] D. Sekyi-Arthur, S.Y. Mensah, E.K. Amewode, C. Jebuni-Adanu, J. Asare, High frequency amplification of acoustic phonons in fluorine-doped single-walled carbon nanotubes, Diam. Relat. Mater. (2023) 110642.
[19] D. Sekyi-Arthur, S.Y. Mensah, E.K. Amewude, R. Arthur, R.R. Adams, Acousto-electric direct current density in fluorine doped single-walled carbon nanotubes due to harmonic mixing of bichromatic fields with commensurate frequencies, Diam. Relat. Mater. (2023) 109993.
[20] M.S. Dresselhaus, G. Dresselhaus, P. Avouris, Carbon Nanotubes: Synthesis, Structure, Properties and Applications, Springer, Berlin, 2001.
[21] W. Mickelson, I.W. Chiang, J.L. Zimmerman, P.J. Boul, J. Lozano, J. Liu, R.E. Smalley, R.H. Hauge, J.L. Margrave, Fluorination of single-walled carbon nanotubes, Chem. Phys. Lett. 296 (1–2) (1998) 188–194, http://dx.doi.org/10.1016/S0009-2614(98)01123-2.
[22] I.Y. Jeon, J.G. Kim, H.J. Choi, J. Yu, J.B. Baek, Fluorinated carbon nanotubes: Synthesis and characterization, J. Mater. Chem. 17 (47) (2007) 4923–4928, http://dx.doi.org/10.1039/B711136A.
[23] S.A. Ktitorov, G.S. Simin, V. Ya Sindalovskii, Bragg reflections and the high-frequency conductivity of an electronic solid-state plasma, Sov. Phys.–Solid State 13 (8) (1972) 1872–1874.
[24] Kogan, Sh. M., Electronic Noise and Fluctuations in Solids, Cambridge University Press, Cambridge, 1970.
[25] R. Saito, G. Dresselhaus, M.S. Dresselhaus, Physical Properties of Carbon Nanotubes, Imperial College Press, London, 1998.
[26] S. Baroni, S. de Gironcoli, A. Dal Corso, P. Giannozzi, Phonons and related crystal properties from density-functional perturbation theory, Rev. Modern Phys. 73 (2) (2001) 515–562, http://dx.doi.org/10.1103/RevModPhys.73.515.
[27] P. Giannozzi, S. Baroni, N. Bonini, M. Calandra, R. Car, C. Cavazzoni, D. Ceresoli, G.L. Chiarotti, M. Cococcioni, I. Dabo, A. Dal Corso, S. de Gironcoli, S. Fabris, G. Fratesi, R. Gebauer, U. Gerstmann, C. Gougoussis, A. Kokalj, M. Lazzeri, L. Martin-Samos, N. Marzari, F. Mauri, R. Mazzarello, S. Paolini, A. Pasquarello, L. Paulatto, C. Sbraccia, S. Scandolo, G. Sclauzero, A.P. Seitsonen, A. Smogunov, P. Umari, R.M. Wentzcovitch, QUANTUM ESPRESSO: A modular and open-source software project for quantum simulations of materials, J. Phys.: Condens. Matter. 21 (39) (2009) 395502, http://dx.doi.org/10.1088/0953-8984/21/39/395502.
[28] R.M. Martin, Electronic Structure: Basic Theory and Practical Methods, Cambridge University Press, Cambridge, 2004.
[29] D. Sekyi-Arthur, S.Y. Mensah, K. Wi-Adu, K.A. Dompreh, R. Edziah, Tunable high-frequency acoustoelectric current oscillations in fluorine-doped single-walled carbon nanotubes, J. Nanotechnol. 2024 (2024) http://dx.doi.org/10.1155/2024/7426184.
[30] B.K. Ridley, Quantum Processes in Semiconductors, 5th ed., Oxford University Press, Oxford, ISBN: 978-0-19-967721-4, 2013.
[31] M. Lundstrom, Fundamentals of Carrier Transport, 5th ed., Cambridge University Press, Cambridge, 2000.
[32] G. Weinreich, Acoustoelectric effects in semiconductors, Phys. Rev. 104 (2) (1956) 321–324, http://dx.doi.org/10.1103/PhysRev.104.321.
[33] A.R. Hutson, D.L. White, Elastic wave propagation in piezoelectric semiconductors, J. Appl. Phys. 32 (5) (1961) 779–782, http://dx.doi.org/10.1063/1.1736117.
[34] E. Pop, D. Mann, Q. Wang, K. Goodson, H. Dai, Thermal conductance of an individual single-wall carbon nanotube above room temperature, Nano Lett. 6 (1) (2006) 96–100, http://dx.doi.org/10.1021/nl052145f.
[35] D.P. Morgan, Surface Acoustic Wave Filters: With Applications To Electronic Communications and Signal Processing, 2nd ed., Academic Press, Amsterdam, 2007.
[36] A.A. Clerk, K.W. Lehnert, P. Bertet, J.R. Petta, Y. Nakamura, Hybrid quantum systems with circuit quantum electrodynamics, Nat. Phys. 16 (3) (2020) 257–267, http://dx.doi.org/10.1038/s41567-020-0797-9.